NeuroImage 271 (2023) 119988

Contents lists available at ScienceDirect

NeuroImage

journal homepage: www.elsevier.com/locate/neuroimage

Cognition/ Aging

Investigating Intra-Individual Networks of Response Inhibition and Interference Resolution using 7T MRI

S.J.S. Isherwood[1,*], PL. Bazin[1,2], S. Miletić[1], N.R. Stevenson[1], A.C. Trutti[1,3], D.H.Y. Tse[4], A. Heathcote[5], D. Matzke[5], R.J. Innes[1], S. Habli[4], D.R. Sokołowski[4], A. Alkemade[1], A.K. Håberg[4], B.U. Forstmann[1]

[1] *Integrative Model-Based Cognitive Neuroscience Research Unit, University of Amsterdam, Amsterdam, The Netherlands*
[2] *Department of Neurophysics, Max Planck Institute for Human Cognitive and Brain Sciences, Leipzig, Germany*
[3] *Institute of Psychology, Leiden University, Leiden, The Netherlands*
[4] *Norwegian University of Science and Technology, Trondheim, Norway*
[5] *Department of Psychological Methods, University of Amsterdam, Amsterdam, The Netherlands*

ARTICLE INFO

Keywords:
Ultra-high field MRI
basal ganglia
inhibition
interference
cognitive modelling
fMRI

ABSTRACT

Response inhibition and interference resolution are often considered subcomponents of an overarching inhibition system that utilizes the so-called cortico-basal-ganglia loop. Up until now, most previous functional magnetic resonance imaging (fMRI) literature has compared the two using between-subject designs, pooling data in the form of a meta-analysis or comparing different groups. Here, we investigate the overlap of activation patterns underlying response inhibition and interference resolution on a within-subject level, using ultra-high field MRI. In this model-based study, we furthered the functional analysis with cognitive modelling techniques to provide a more in-depth understanding of behaviour. We applied the stop-signal task and multi-source interference task to measure response inhibition and interference resolution, respectively. Our results lead us to conclude that these constructs are rooted in anatomically distinct brain areas and provide little evidence for spatial overlap. Across the two tasks, common BOLD responses were observed in the inferior frontal gyrus and anterior insula. Interference resolution relied more heavily on subcortical components, specifically nodes of the commonly referred to *indirect* and *hyperdirect* pathways, as well as the anterior cingulate cortex, and pre-supplementary motor area. Our data indicated that orbitofrontal cortex activation is specific to response inhibition. Our model-based approach provided evidence for the dissimilarity in behavioural dynamics between the two tasks. The current work exemplifies the importance of reducing inter-individual variance when comparing network patterns and the value of UHF-MRI for high resolution functional mapping.

1. Introduction

Response inhibition is defined as the global inhibition of a planned or already initiated response, commonly investigated using the stop-signal task (SST; Aron, 2011; Logan & Cowan, 1984). Interference resolution is a selective inhibition process that functions to suppress prepotent but suboptimal behaviour and is required for tasks such as the multi-source interference task (MSIT; Bush et al., 2003). Although both constructs are placed under the umbrella of inhibition-related functioning, concrete knowledge on their overlap in neural implementation is lacking (Isherwood, et al., 2021; Nee et al., 2007; Schmidt et al., 2020; Swick et al., 2011). Both the SST and MSIT have yielded robust results in functional magnetic resonance imaging (fMRI) studies and lend themselves well to cognitive modelling, although the neural architectures underlying behaviour in the tasks have not been directly compared (Bush & Shin, 2006; de Hollander et al., 2017; Deng et al., 2018; Miletić et al., 2020).

Accumulating evidence indicates response inhibition is executed via a complex cortico-basal-ganglia network which is also involved in action planning and initiation (Albin et al., 1989; DeLong, 1990; Jahanshahi et al., 2015; Wessel & Aron, 2017), though some work has revealed inconsistencies in this theory (de Hollander et al., 2017; Miletić et al., 2020). Through these intricate subcortical-cortical connections the idea is that the *direct* pathway plays a pivotal role in the initiation of movement (see Fig. 1). It is generally accepted that two separate pathways, the *indirect* and *hyperdirect*, work in tandem to pause or inhibit planned or already initiated movement (Diesburg & Wessel, 2021; Schmidt & Berke, 2017). While the role of this network in response in-

* Corresponding author: University of Amsterdam (UvA) REC-G, Room 3.03, Nieuwe Achtergracht 129B, 1001 NK, Amsterdam
E-mail address: s.j.s.isherwood@uva.nl (S.J.S. Isherwood).

https://doi.org/10.1016/j.neuroimage.2023.119988.
Received 21 October 2022; Received in revised form 20 February 2023; Accepted 25 February 2023
Available online 1 March 2023.

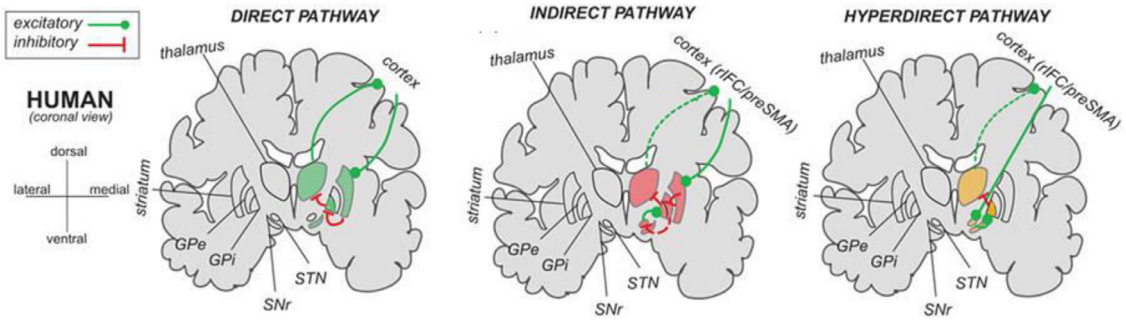

Figure 1. The *direct, indirect* and *hyperdirect* pathways in humans (adapted from Diesburg & Wessel, 2021). Glutamatergic connections are represented as green lines, GABAergic connections as red and a reduction in signaling as dotted. IFG, inferior frontal gyrus; preSMA, pre-supplementary motor area; GPe, globus pallidus externa; GPi, globus pallidus interna; SNr, substantia nigra pars reticulata; STN, subthalamic nucleus.

hibition has been widely investigated, its role in interference resolution remains elusive. With the idea that interference resolution is a type of selective inhibition, and response inhibition a more global method of inhibition, we sought to investigate to what extent they share common neural substrates within and outside of these canonical inhibitory pathways.

Previous meta-analyses and original studies indicate that the two types of inhibitory control utilize several distinct brain areas, namely the pre-supplementary motor area (preSMA) and subthalamic nucleus (STN) in response inhibition and the anterior cingulate cortex (ACC), superior parietal lobule (SPL) and striatum in interference resolution (Cieslik et al., 2015; Hung et al., 2018). However, overlapping activation has been found in the anterior insula (aI), preSMA, and inferior frontal gyrus (Cieslik et al., 2015; Hung et al., 2018; Isherwood, et al., 2021). These studies also suggest that response inhibition recruits a more right-lateralized, and interference resolution a more left-lateralized network. Combined, these studies found little evidence of common subcortical involvement across the tasks. It is important to note that almost all meta-analyses are based mostly on 1.5T or 3T data and may lack the signal quality (in terms of signal-to-noise ratios) necessary to uncover activation in deeper parts of the brain. As such, there is an abundance of studies investigating both response inhibition and interference resolution in isolation, but few that have focused on intra-individual overlaps (Sebastian et al., 2013), especially at higher field strengths.

In addition to a lack of within-subject studies, model-based imaging approaches are missing (Sebastian et al., 2018; van Maanen et al., 2015). Such an approach allows us to further understand the algorithmic level underlying behaviour as well as the implementation level in the brain (Marr, 1982), giving us the tools to gain mechanistic understanding. For example, if a parameter of a cognitive model correlates with brain activity in a specific region, there is an indication that the region could be involved in the specific process that parameter defines. To gain a deeper understanding of the neural signatures of response inhibition and interference resolution, here we apply both a well-established and a novel method of cognitive modelling to the two tasks (Matzke et al., 2013, 2017). The stop-signal reaction time (SSRT) is the canonical marker of behavioural stopping ability during the SST and can be estimated using several methods (Logan et al., 1984; Matzke et al., 2018). This marker has been shown to correlate negatively with nodes of the *indirect* pathway including the rIFG, caudate nucleus, and STN activity (Aron & Poldrack, 2006; Li et al., 2006; Whelan et al., 2012). To the best of our knowledge, there are no model-based fMRI studies of the MSIT. Here, we apply an evidence accumulation model, the racing Wald, to identify whether we can capture behaviour during interference resolution in terms of changes in drift rate, threshold or non-decision time (Logan et al., 2014; Stevenson et al., 2022).

To accurately compare these two tasks, we employed ultra-high field magnetic resonance imaging (UHF-MRI) to acquire within-subject fMRI data of the SST and MSIT. UHF-MRI allowed us to obtain high resolution and optimized contrasts in deep subcortical areas as well as maintaining sufficient signal in the cortex (Isherwood et al., 2021; Miletić et al., 2020). The echo time is important for optimal BOLD-sensitivity and should be equal to the $T2^*$ of the tissue of interest, for the STN and GPe this is around 14 ms (Posse et al., 1999). We therefore 'tailored' the sequence to the subcortex, by choosing a TE more optimal for it (Miletić et al., 2020). This, of course, results in a suboptimal TE for imaging cortical regions (which is around 30 ms). Due to the increased signal you achieve in the cortex, simply from being closer to the MRI head coils, we chose to focus on increasing sensitivity to subcortical BOLD responses which are widely underrepresented in functional studies.

We fit both whole-brain and region of interest (ROI) based general linear models (GLMs) for each participant of the study and compared their activation patterns. As the precise delineation of smaller subcortical structures is crucial for accurate statistical analysis, we here used the multi-contrast anatomical subcortical structures parcellation (MASSP) algorithm to directly obtain individual masks for each participant (Bazin et al., 2020). To better understand the mechanisms underlying observed behaviour in each task, we utilized separate cognitive modelling techniques. Based on previous literature, we expected to replicate findings of cortical overlap of response inhibition and interference resolution in the aI, preSMA, and IFG. Additionally, by using the high-resolution subcortical masks derived we aimed to explore possible commonalities in basal ganglia structures that constitute canonical inhibitory pathways.

2. Methods

2.1. Participants

A total of 37 participants (20 female; mean age 26.3 ± 5.6; age range 19 – 39 years) completed the study, which was approved by the ethical committee at the University of Amsterdam, the Netherlands, and the Regional Committees for Medical and Health Research Ethics, Norway. Written informed consent and MRI screening forms were obtained from all participants. The participants were recruited from the Norwegian University of Science and Technology and had corrected-to-normal vision and no history of epilepsy or overt clinical neuropsychiatric disease.

2.2. Scanning protocols

Each participant was scanned in a total of four MR sessions as part of a larger project on a Siemens MAGNETOM TERRA (Tesla (T) = 7; gradient strength = 80 mT/m at 200 T/m/s) with a 32-channel head coil. Here, we only describe the sessions that acquired the high resolution anatomical images and the SST and MSIT experimental data. The anatomical session acquired a multi-echo gradient recalled echo scan (GRE; TR = 31.0 ms, TE1 = 2.51 ms, TE2 = 7.22 ms, TE3 = 14.44 ms, TE4 = 23.23 ms, FA= 12°, FOV = 240 × 240 × 168 mm) and an

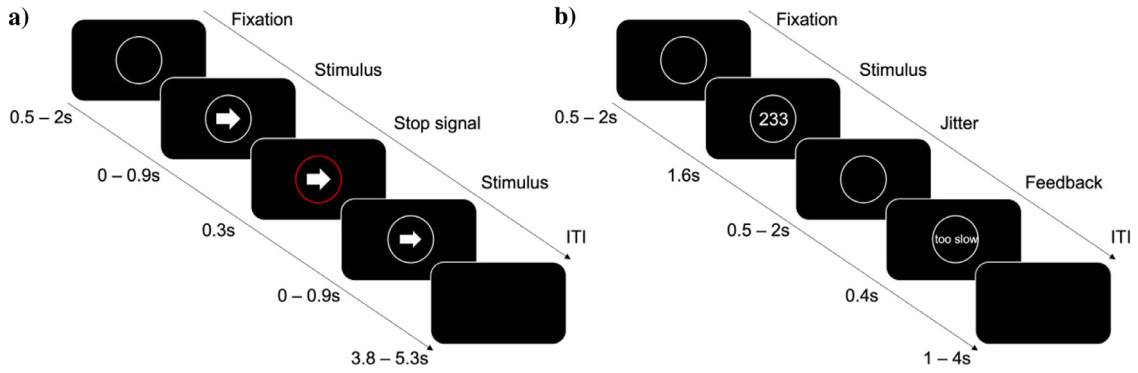

Figure 2. Task design of the SST (left) and MSIT (right). Trials in the SST lasted 7 seconds and were either *go* or *stop* trials: **a)** shows an example of a stop trial, where the participant should have attempted to inhibit responding to the right facing arrow. Trials in the MSIT also lasted 7 seconds. **b)** An example of an incongruent trial, where the correct response is 2 (middle finger on the button box).

MP2RAGE scan (TR = 4300 ms; TE = 1.99 ms; inversions TI1 = 840 ms, TI2 = 3270 ms; flip angle 1 = 5°, flip angle 2 = 6°Field of View (FOV) = 240 × 240 × 168 mm; bandwidth (BW) = 250 Hz/Px; Marques et al., 2010). The experimental session consisted of four functional echo-planar imaging runs with subsequent acquisition of 4 EPI volumes with opposite phase encoding direction for susceptibility distortion purposes. The functional data was collected using a single echo 2D-EPI BOLD sequence (TR = 1380 ms; TE = 14 ms; MB = 2; GRAPPA = 3; voxel size = 1.5 mm isotropic; partial Fourier = 6/8; flip angle = 60°; MS mode = interleaved; FOV = 192 × 192 × 128 mm; matrix size = 128 × 128; BW = 1446 Hz/Px; slices = 82; phase encoding direction = A >> P; echo spacing = 0.8 ms). Each task had a total of 2 runs, each with a 13:27 min acquisition time, for a total of 4 runs and 53:48 min functional scanning.

2.3. Physiological data

Physiological data (heart and breathing rate) were recorded for all participants in order to estimate the effects of physiological noise on the fMRI data. An 18 regressor RETROICOR model was fit (Glover et al., 2000). This included a fourth order phase Fourier expansion of the heart rate signal, second order phase expansion of the respiration signal, and a second order phase Fourier expansion of the interaction between heart rate and respiration (Harvey et al., 2008). Additional regressors were used to model heart rate variability (HRV; Chang et al., 2009), and respiratory volume per time unit (RVT; Birn et al., 2008; Harrison et al., 2021).The PhysIO toolbox (Kasper et al., 2017) as executed in the TAPAS software (Frässle et al., 2021) was used for physiological regressor estimation.

2.4. Experimental Paradigms

2.4.1. Stop Signal Task (SST)

To test response inhibition, we used the SST(Logan & Cowan, 1984; Verbruggen, et al., 2019). Participants were presented with a right or left-facing arrow surrounded by a white circle in the middle of the screen. They were instructed to respond to the direction of the arrow as quickly and as accurately as possible, using the index finger on their left or right hand (see Fig. 2). 25% of the trials were 'stop' trials, where the circle surrounding the stimulus turned red. The other 75% of the trials are termed 'go' trials, where the circle remains white. When presented with a stop trial, participants were instructed to inhibit their response to the direction of the arrow. On go trials, participants should respond to the arrow as initially instructed. The time delay between the presentation of the arrow stimulus on stop trials and the visual stop signal (the red circle), is defined as the stop signal delay (SSD). The SSD was adjusted to the stopping ability of the participant by means of a staircase procedure, where the SSD is increased 50ms if the participant successfully stopped and decreased by 50ms when the participant failed to stop. The SSD was initially set at 200ms for all participants. For analysis, trials were categorized into go trials (GO; no visual stop signal cue), successful stops (SS; visual cue presented, and response inhibited) and failed stops (FS; visual cue presented but response still initiated).

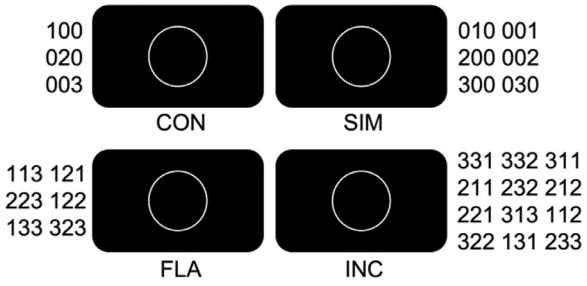

Figure 3. Conditions and stimuli presented in the MSIT. Possible stimuli are shown left or right of the conditions. There were three possible stimuli in the CON condition, six possible stimuli in the SIM and FLA conditions, and twelve possible stimuli in the INC condition. Each subject was presented with three selected stimuli from each condition during the experiment. CON, congruent; SIM, Simon; FLA, Flanker; INC, incongruent.

2.4.2. Multi-source Interference Task (MSIT)

To test interference resolution, we used the MSIT (Bush et al., 2003). Participants were presented with three numbers inside a white circle in the middle of the screen (see Fig. 2). Of these three numbers, two were identical and one differed. These numbers could either be a 0, 1, 2 or 3. Participants responded by indicating the identity, but not the position, of the number that was the odd one out as quickly and accurately as possible using the index, middle and ring fingers of their right hand. For example, the correct response to the stimulus '1 3 1' was to press the button corresponding to the number 3. There were four conditions; congruent (CON), Simon (SIM), Flanker (FLA), and incongruent (INC; see Fig. 3).

CON trials incurred stimuli such as '1 0 0' or '0 2 0', in which the correct responses were 1 and 2, respectively, and include a congruency between position and identity of the correct response. SIM trials contained stimuli such as '0 0 1' or '2 0 0', where the correct responses were also 1 and 2, respectively. The Simon effect caused an inconsistency between the position and identity of the correct answer, increasing the difficulty of the choice. FLA trials contained stimuli such as '1 2 2' or '3 2 3', in which the correct responses were 1 and 2, respectively. FLA trials also include a congruency between the position and identity of the correct response, but this response was surrounded by goal-irrelevant stimuli which act as distractors, which further increases choice difficulty, known as the Flanker effect. Finally, INC trials contained stimuli

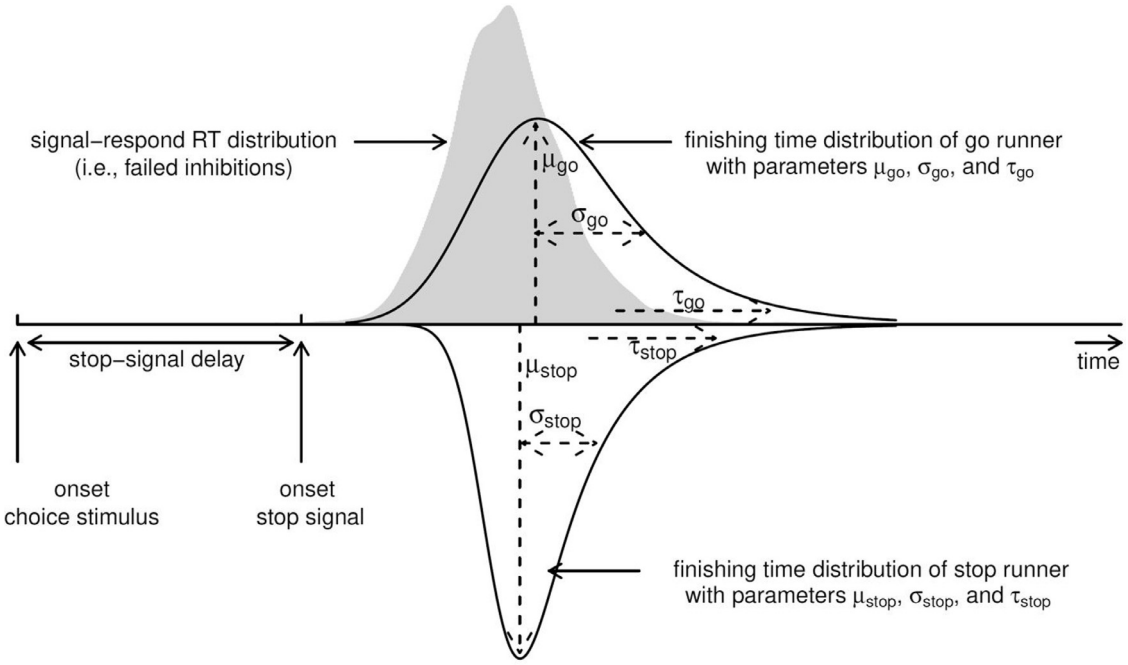

Figure 4. Schematic representation of the horse-race model (Heathcote et al., 2019). The horse-race model treats go RTs and SSRTs as independent random variables, defining the finishing times of either the go or the stop process. The signal-response RT (SRRT) distribution (grey) is treated as a censored Go RT distribution. If the go RT on any given trial is longer than SSD + SSRT, the response is successfully inhibited. SRRTs occur when the go RT on the given trial is shorter than SSD + SSRT. Figure available at tinyurl.com/5hnyzz2w under CC-BY 2.0 license (https://creativecommons.org/licenses/by/2.0/).

such as '3 3 1' or '1 1 2', with correct answers as 1 and 2, respectively. In INC trials, both the Simon and Flanker effects were present. We defined interference effects as a bias towards a possible choice option that is incorrect, the CON condition therefore had no interference effects, as the zeros did not bias participants towards a potential or valid response option. As there were different numbers of possible stimuli in each condition (e.g., three for the CON condition but twelve for the INC condition), each participant was pseudorandomly assigned three stimuli from each condition as to harmonize any learning effects. After the response window, feedback of either 'in time' (responses less than 600ms), 'too slow' (responses between 600 – 900ms) or 'very slow' (for response more than 900ms) was shown. This feedback was aimed to keep participants responding quickly.

2.5. Behavioural Analyses

For both runs of the SST, median reaction times (RTs) on *go* and *stop* trials, the mean stop-signal delay (SSD) and proportion of *successful stops* (SS) were calculated. For each participant, the main measure of response inhibition, the stop-signal reaction time (SSRT) were calculated using modelling techniques described below. For both runs of the MSIT, median RTs and accuracy were calculated for all four conditions. Bayes factors (BFs) were computed using the BayesFactor package (Morey & Rouder, 2015).

2.6. Cognitive Modelling

2.6.1. SST

The SST was modelled using the Bayesian Estimation of Ex-Gaussian Stop-Signal (BEESTS) reaction time distributions method (Matzke et al., 2013, 2017). The aim of modelling the SST is to estimate the efficiency of the unobservable stopping response, commonly defined as the stop signal reaction time (SSRT). The model is based on the standard horse-race model (see Fig. 4), where the *go* process, initiated upon presentation of the stimulus, and the *stop* process, initiated by the presentation of the visual stop signal, independently race against each other. If the *go* process finishes the race first, the prepared action is executed. If the *stop* process finishes first, this action is inhibited. This can be further formalized, if the *go* RT is faster than the SSD + SSRT on a given trial, then the *go* process wins and a signal-response RT (SRRT) is observed. If the *go* RT is slower than the SSD + SSRT, then the stop process wins, and the action is inhibited. The RT distribution derived from *failed stop* trials are estimated as a partially known (censored) *go* RT distribution. The race model assumes that, on average, these SRRTs are quicker than go RTs. Due to the simplicity of the go choice, incorrect response on go trials were removed from the analysis (0.24% of all go data).

By using a Bayesian parametric approach (BPA), the entire distribution of SSRTs is estimated, as opposed to using the mean or median approach, which provides only a summary measure. The BPA assumes that *go* RTs and SSRTs follow an ex-gaussian distribution (Matzke & Wagenmakers, 2009; Ratcliff & Murdock, 1976). Such a distribution is defined by three parameters, the mean of the gaussian component (μ), the standard deviation of the gaussian component (σ) and the mean of the exponential component (τ). The BPA model simultaneously estimates the *go* (μ_{go}, σ_{go}, τ_{go}) and *stop* (μ_{stop}, σ_{stop}, τ_{stop}) RT distribution parameters. The mean of the ex-gaussian distribution is the sum of the μ and τ parameters, $\mu_{go} + \tau_{go}$ derives the mean go RT and $\mu_{stop} + \tau_{stop}$ derives the mean SSRT. Posterior distributions for these *go* and *stop* parameters are estimated using Markov chain Monte Carlo sampling (Gilks et al., 2003). Proper convergence of these chains during sampling is diagnosed using the Gelman-Rubin statistic, where values of 1.1 or lower indicate the chains have converged (Gelman & Rubin, 1992). The stop signal data is analyzed hierarchically, therefore assuming that subject-level *go* and *stop* signal parameters are drawn from group-level distributions. Both group-level and subject-level parameters are estimated simultaneously, where the group-level distributions define the between-subject variability of the subject-level parameters (Gelman & Hill, 2006). Hierarchical methods allow adjustment or "shrinkage" of extreme or unlikely parameters estimates towards the group mean.

Attentional failures are captured by the model by means of trigger failures (tf), where the *stop* process is not initiated and *go* failures (gf), where the go process is not initiated. The overall probability of stopping

remains the same, as stopping and trigger failures are, by definition, mutually exclusive. Similarly, *go* responses are not observed upon the manifestation of a *go*-failure. The priors used for the population-level parameters of the model were truncated normal distributions, constrained between 0 and 1000ms for the *go* and *stop* parameters and normal distributions between -6 and 6 for P(tf) and P(gf) parameters. The priors for the group-level means and group-level standard deviations are weakly informative uniform distributions, as in (Matzke et al., 2017). After model estimation, an inverse probit transformation that simultaneously considers the population-level mean and the population-level standard deviation was applied to the P(tf) and P(gf) parameters to convert them to the probability scale. The described model is therefore comprised of 8 parameters (μ_{go}, σ_{go}, τ_{go}, μ_{stop}, σ_{stop}, τ_{stop}, P(tf), P(gf)).

2.6.2. MSIT

There have been few attempts to investigate the MSIT within a model-based framework. Here, we use a process-orientated approach developed by Stevenson et al., (2022) to model participant behaviour during the task. Through cognitive modelling, the aim is to disentangle the individual contribution that both the Simon and Flanker effects have on behaviour, as well as their cumulative effects when both are present. The evidence accumulation model we used was the racing Wald model (Logan et al., 2014). This model is characterized by three parameters: the rate of evidence accumulation (drift rate), the decision threshold (B) and non-decision time (t0). We assume that evidence accumulates during each trial of the task at some rate until evidence for a certain decision reaches a threshold, upon which a decision is triggered. The model assumes that most of the between-condition effects can be put down to differences in drift rates. Since there are three potential responses, there are three accumulators racing on each trial. As a reminder, there are four conditions in this task, a CON condition (no Simon or Flanker), SIM condition (Simon only), FLA condition (Flanker only) and INC condition (both Simon and Flanker). We hypothesized that the drift rate for each choice is jointly driven by an urgency component and the evidence supporting that choice. The drift rate for any choice is therefore an addition of the urgency component (v_0), target evidence (v_{Target}), Simon evidence (v_{Simon}), and Flanker evidence (v_{Flank}). Furthermore, we also found that response time and accuracy were influenced by the position of the target, possibly due to left to right reading effects (Stevenson et al., 2022). We therefore modified the drift rate of the accumulator corresponding to the target based on position of the target. Additionally, the evidence accumulation process is subject to Gaussian noise W, with standard deviation σ, defining within-trial variation in drift rate, was fixed to 1 to satisfy scaling constraints. Consequently, the drift rate in our MSIT model can be described as:

$$dx_A = \left[V_0 + v_{Flank} + v_{Simon} + v_{Correct}\right]dt + \sigma W$$

Where, v_{Correct} is equal to the summation of v_{Target} and the positional drift rate modifier, which can vary among positions (1, 2 or 3). The positional drift rate modifier v_{pos3} was fixed to 0, by which the other positional modifiers (v_{pos1} and v_{pos2}) were relative. In total our MSIT model comprised 8 estimated parameters (v_{Flank}, v_{Simon}, v_{Target}, v_{pos1}, v_{pos2}, v_0, B, t0). The above-described model was selected after model comparison against competing models as in Stevenson et al., (2022). Uninformed priors were used for all parameters constituting a Gaussian distribution centred on 0 with a standard deviation of 1.

2.7. Procedure and exclusions

Prior to the MRI session, all participants completed a practice version of the two tasks to ensure that the task instructions were correctly understood. Each trial of the functional tasks lasted 7 seconds. For the SST, six participants were excluded on the basis of having (1) more than 10 go-omissions (non-responsive during Go trials) across both runs. One of these participants also had (2) a stopping accuracy of less than 35% or more than 65%. No participants were excluded for having (3) a go-accuracy of less than 95%. Two of the already excluded participants had (4) mean signal respond RTs that were longer on average than go RTs (inconsistent with the race model; (Logan et al., 1984). For the MSIT, participants were excluded if they performed below chance level (33%) in any of the four conditions. One subject was excluded for using incorrect response buttons. Based on these exclusions the final sample for the analysis was a total of 31 participants for the SST (17 female; mean age 26.7 ± 5.9; age range 19 -39) and 36 participants for the MSIT (19 female; mean age 26.4 ± 5.7; age range 19 - 39).

2.8. fMRI preprocessing pipeline

fMRIPrep was used to preprocess all acquired anatomical and functional data (Esteban et al., 2018, 2020). For each of the 2 BOLD runs found per task per subject, the following preprocessing was performed. First, a reference volume and its skull-stripped version were generated by aligning and averaging 1 single-band references (SBRefs). A B0-nonuniformity map (or *fieldmap*) was estimated based on two echo-planar imaging (EPI) references with opposing phase-encoding directions, with *3dQwarp* (Cox and Hyde, 1997; AFNI 20160207). Based on the estimated susceptibility distortion, a corrected EPI (echo-planar imaging) reference was calculated for a more accurate co-registration with the anatomical reference. The BOLD reference was then co-registered to the T1w reference using *bbregister* (FreeSurfer) which implements boundary-based registration (Greve & Fischl, 2009). Co-registration was configured with six degrees of freedom. Head-motion parameters with respect to the BOLD reference (transformation matrices, and six corresponding rotation and translation parameters) are estimated before any spatiotemporal filtering using mcflirt (FSL 5.0.9, Jenkinson et al., 2002). BOLD runs were slice-time corrected using *3dTshift* from AFNI 20160207 (Cox and Hyde, 1997; RRID:SCR_005927). First, a reference volume and its skull-stripped version were generated using a custom methodology of *fMRIPrep*. The BOLD time-series (including slice-timing correction when applied) were resampled onto their original, native space by applying a single, composite trans- form to correct for head-motion and susceptibility distortions. These resampled BOLD time-series will be referred to as *preprocessed BOLD in original space*, or just *preprocessed BOLD*. Several confounding time-series were calculated based on the *preprocessed BOLD*: framewise displacement (FD), DVARS (the spatial standard deviation of difference images), and three region-wise global signals. FD was computed using two formulations following Power (absolute sum of relative motions, Power et al., 2014) and Jenkinson (relative root mean square displacement between affines, Jenkinson et al., 2002). FD and DVARS are calculated for each functional run, both using their implementations in *Nipype* (following the definitions by Power et al., 2014). The three global signals are extracted within the CSF, the WM, and the whole-brain masks. Additionally, a set of physiological regressors were extracted to allow for component-based noise correction (*CompCor*, Behzadi et al., 2007). Principal components are estimated after high-pass filtering the *preprocessed BOLD* time-series (using a discrete cosine filter with 128 s cut-off) for the two *CompCor* variants: temporal (tCompCor) and anatomical (aCompCor). tCompCor components are then calculated from the top 2% variable voxels within the brain mask. For aCompCor, three probabilistic masks (CSF, WM and combined CSF + WM) are generated in anatomical space. The implementation differs from that of Behzadi et al. in that instead of eroding the masks by 2 pixels on BOLD space, the aCompCor masks are subtracted a mask of pixels that likely contain a volume fraction of GM. This mask is obtained by dilating a GM mask extracted from the FreeSurfer's *aseg* segmentation, and it ensures components are not extracted from voxels containing a minimal fraction of GM. Finally, these masks are resampled into BOLD space and binarized by thresholding at 0.99 (as in the original implementation). Components are also calculated separately within the WM and CSF masks. For each CompCor decomposition, the *k* components with the largest singular values are re-

tained, such that the retained components' time series are sufficient to explain 50 percent of variance across the nuisance mask (CSF, WM, combined, or temporal). The remaining components are dropped from consideration. The head-motion estimates calculated in the correction step were also placed within the corresponding confounds file. The confound time series derived from head motion esti- mates and global signals were expanded with the inclusion of temporal derivatives and quadratic terms for each (Satterthwaite et al., 2013). Frames that exceeded a threshold of 0.5 mm FD or 1.5 standardised DVARS were annotated as motion outliers. All resam- plings can be performed with *a single interpolation step* by composing all the pertinent transformations (i.e. head-motion transform matrices, susceptibility distortion correction when available, and co-registrations to anatomical and output spaces). Gridded (volumetric) resamplings were performed using antsApplyTransforms (ANTs), configured with Lanczos interpolation to minimize the smoothing effects of other kernels (Lanczos, 1964). Non-gridded (surface) resamplings were performed using mri_vol2surf (FreeSurfer). Many internal operations of *fMRIPrep* use *Nilearn* 0.6.2 (Abraham et al., 2014, RRID:SCR_001362), mostly within the functional processing workflow.

2.9. fMRI analyses

2.9.1. General Linear Models (GLMs)

GLM analyses were performed at both a whole-brain voxel-wise and region-specific level. A canonical double gamma hemodynamic response function (HRF) with temporal derivative was used as the basis set for both tasks and both methods of analysis (Glover, 1999). The design matrix consisted of either the three experimental conditions for the SST (GO, FS, SS) or the four for the MSIT (CON, SIM, FLA, INC). Functional data were first spatially smoothed using SUSAN (kernel size full width half maximum = 1.5 mm) and high-pass filtered before GLM analysis (Smith & Brady, 1997). In addition to the task-specific regressors, six motion parameters were also included (three translational and three rotational) as well as DVARS and framewise displacement estimated during preprocessing. 20 physiological regressors obtained from RETROICOR estimations were also included in the design matrix. For two participants on the second runs of the SST physiological data were not collected due to technical reasons, the first 20 aCompCor components were used instead (Behzadi et al., 2007). Therefore, a total of 31 or 32 regressors were used in the model, depending on the task being analyzed (SST or MSIT, respectively). The SST consists of three possible contrasts: *FS - GO, FS - SS* and *SS - GO*. The MSIT consists of six possible contrasts: *INC - CON, INC - SIM, INC - FLA, SIM - CON, SIM - FLA* and *FLA - CON*.

Whole-brain analyses were computed using the FILM method from FSL FEAT (Jenkinson et al., 2012; Woolrich et al., 2001), accounting for autocorrelated residuals. Fixed effects analyses were used to combine the resulting run-level GLMs per task. Group-level models were subsequently estimated using FLAME1 and FLAME2 from FSL (Woolrich et al., 2001). Statistical parametric maps (SPMs) were generated to visualize the resulting group-level models. The maps were corrected for the false discovery rate (FDR) using critical value of $q < 0.05$ (Yekutieli & Benjamini, 1999).

Region of interest (ROI) analyses were then performed. Timeseries were extracted from each subcortical region of interest using probabilistic masks provided by MASSP (Bazin et al., 2020), each voxels contribution to the mean signal of the region was therefore weighted by its probability of belonging to the region. Cortical regions parcellations were provided by the Harvard-Oxford cortical atlas (Rizk-Jackson et al., 2011). The timeseries were subsequently converted to percentage signal change by dividing each timepoint by the mean timeseries signal, multiplying by 100 and subtracting 100. These timeseries were extracted from unsmoothed data so to ensure regional specificity. Runs were concatenated within task. We only infer from positive BOLD responses due to the discrepancy around negative BOLD responses (Schridde et al., 2008; Wade, 2002).

2.9.2. Comparisons

To investigate the similarities and differences in neural implementation during the two tasks, we performed both a conjunction and subtraction analysis on the GLMs. To do this, we first had to define a contrast for both tasks that best fits the inhibition construct we were measuring. The SS - GO contrast of the SST represents the triggering and successful implementation of the global inhibition pathway, and therefore is the baseline definition of the network behind canonical response inhibition. The INC – CON contrast of the MSIT exemplifies the highest cognitive load of selective inhibition in the task and was therefore used for these analyses. A conjunction map was generated by overlaying the FDR corrected group-level z-maps of the two contrasts and keeping only voxels that survived significance in both instances. For the subtraction analysis, we calculated a voxel-wise comparison of the contrasts by nullifying voxels on the FDR corrected group-level z-map in the MSIT contrast that also survived thresholding in the SST contrast, and vice versa.

In addition to brain-level comparisons, we also investigated behavioural-level associations. To do this, we correlated the model estimates derived from the independent modelling techniques described above. The mean of the group-level parameter estimates were correlated with one another using Pearson's r and FDR corrected to account for multiple comparisons (Pearson, 1895).

3. Results

3.1. Cognitive modelling

3.1.1. SST

To assess the goodness of fit of the model to the data, we plot averaged simulated posterior predictive data and the raw data averaged over all participants (see Fig. 5). The cumulative density functions (CDFs) show the average cumulative probability of observing a correct RT. The sum of each asymptote in each condition equals the probability of making a response. In stop trials, this was around 0.5 due to the frequency of successful stops, where no response is observed. Overall, the model fits the data very well, though it slightly overestimates the RT in STOP conditions. In addition to CDFs referenced above, we also plot the group level inhibition function and median signal-respond RTs (SRRTs). To account for individual differences in participant-specific SSDs, we normalized the inhibition function by averaging equal percentile ranges of SSDs for each participant. As expected, the inhibition function increases with SSD, suggesting that the probability of responding increases as the SSD increases. Additionally, the median SRRTs increased as a function of SSD as expected. The median estimated parameter values and 95% credible intervals for the SST model are as follows; $\mu_{go} = 0.54$ (0.48, 0.59), $\sigma_{go} = 0.08$ (0.05, 0.11), $\tau_{go} = 0.09$ (0.07, 0.11), $\mu_{stop} = 0.21$ (0.20, 0.22), $\sigma_{stop} = 0.01$ (0.0068, 0.031), $\tau_{stop} = 0.018$ (0.0098, 0.043), P(tf) = 0.0062 (0.0019, 0.021), P(gf) = 0.018 (0.011, 0.029), SSRT = 0.23 (0.21, 0.24).

3.1.2. MSIT

To assess goodness of fit of the model and the MSIT data, we compared the average posterior predictive data to the average observed data collected from each participant (see Fig. 6). For accuracy estimates, the model fits each condition relatively well, though it slightly underestimates the accuracy in the INC condition. Estimates for the three quantiles of RT data fit very well, though also underestimating RTs in the INC condition and overestimating the spread of RTs in the SIM condition. Due to the small number of errors in the task, RT data for incorrect responses had a more variable model fit. The mean parameter values and 95% credible intervals for the MSIT model are as follows; $\nu_{Flanker} = 1.25$ (1.06, 1.44), $\nu_{Simon} = 1.31$ (1.09, 1.52), $\nu_{Target} = 3.32$ (3.00, 3.66), $\nu_{pos1} = 0.46$ (0.25, 0.68), $\nu_{pos2} = 0.068$ (-0.09, 0.24), $\nu_0 = -0.08$ (-0.34, 0.19), B = 1.69 (1.57, 1.84), t0 = 0.27 (0.24, 0.29). As shown from the parameter estimates, the $\nu_{Flanker}$ and ν_{Simon} parameters are of similar values suggesting that both types of interference introduce

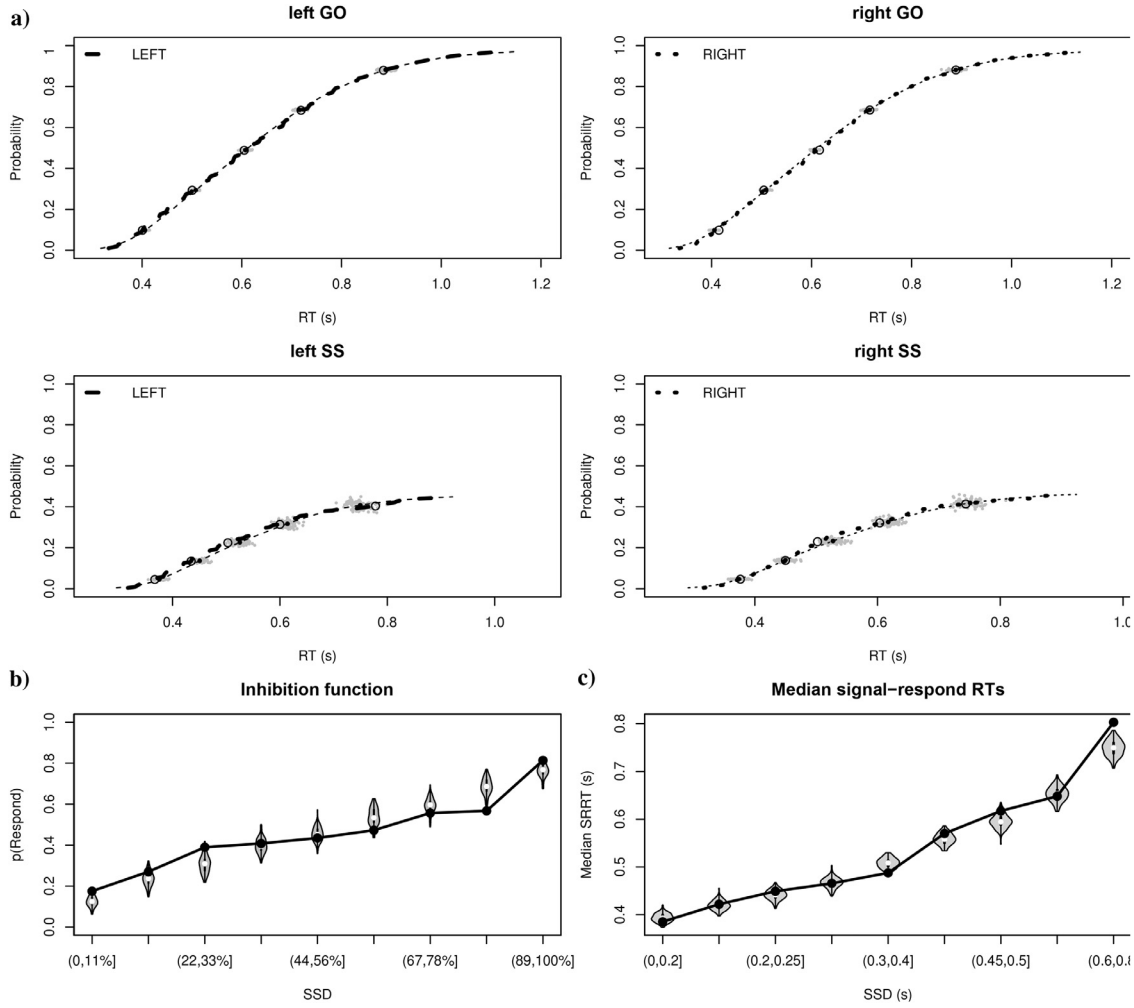

Figure 5. Goodness of fit graphs for the SST. **a)** Cumulative distribution functions. The data are shown with thick lines, with open points marking the 10th, 30th, 50th, 70th, and 90th percentiles. Model predictions are shown with thin lines and solid points, with the clusters of grey dots showing the uncertainty in the percentiles from 100 randomly selected samples from the joint posterior. **b)** Average inhibition function across all participants, as a function of nine equal percentile ranges. **c)** Average median signal response RTs across all participants, as a function of nine time intervals over the range of SSDs for each participant. The data are shown with solid points. The uncertainty of the model predictions resulting from 100 randomly selected samples from the joint posterior is shown with violin plots, with the white dots indicating the median of the predictions.

a similar amount of conflict to resolve. These results indicate that both types of interference biased participants equally.

3.1.3. Comparisons

To identify behavioural associations between the two tasks, we correlated the estimated model parameters within-subject. Fig. 7 shows the results of this analysis. There were no significant correlations in parameter estimates between models after multiple comparison correction. This suggests that the parameters we estimated by decomposing the behavioural data in the two tasks are not linearly dependent.

3.2. Behavioural analyses

3.2.1. SST

The Go RTs for correct responses were within normal range for fMRI studies of response inhibition (Miletić et al., 2020; Verbruggen et al., 2019). Overall, participants had a mean stopping accuracy of 54 ± 1%. Go omissions and Go errors were slightly higher than previous studies (de Hollander et al., 2017; Miletić et al., 2020). SSRT was calculated using the modelling parameters estimated with BEESTS where SSRT is equal to the addition of μ_{stop} and τ_{stop}. Median Go RT did not correlate with estimates of SSRTs when corrected for trigger failures, in accordance with the independence assumption of the independent race model (Aron & Poldrack, 2006; Logan et al., 1984).

3.2.2. MSIT

Table 2 illustrates the differences in RTs and accuracy between the four conditions. All RTs and accuracies were significantly different between conditions based on BFs and FDR correct p-values. Based on FDR-corrected p-values and BFs the differences in RT and accuracy between all conditions were highly significant ($p < 0.001$; $BF > 1e3$) with the exception of the *SIM – FLA* comparisons (RT: $p = 0.003$, $BF = 2.1e1$; Accuracy: $p = 0.006$, $BF = 9.7$).

3.3. GLMs: Whole-brain analyses

3.3.1. SST

3.3.1.1. Task-related activity. For the FS - GO contrast (see Fig. 8) we observed many areas that show significant BOLD responses, in line with previous findings (de Hollander et al., 2017; Miletić et al., 2020; Li et al., 2008). Cortically, these regions included the IFG, preSMA, ACC, and aI. Subcortically, significant differences between the FS and GO trials were found in the caudate nucleus (CN), putamen (PUT), thalamus (Tha),

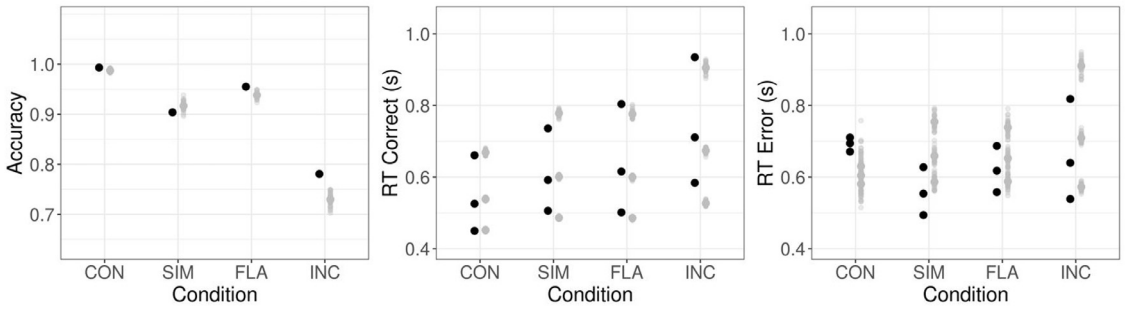

Figure 6. Model fit for accuracy, RTs on correct trials and RTs on error trials in the MSIT. The accuracy graph displays group-level accuracy for each of the four conditions. The RT figures display the 10th, 50th and 90th percentiles for the correct (middle) and error (right) trials. Black denotes the acquired data; shaded grey denotes the model predictions. The uncertainties of the model estimates resulting from 100 randomly selected samples from the joint posterior are denoted by the spread of the shaded area.

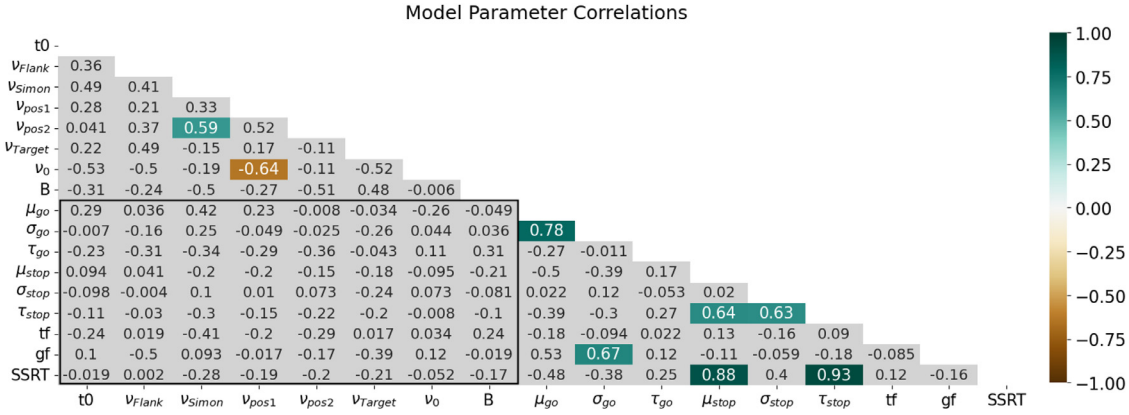

Figure 7. Correlation heatmap depicting associations within and between models for the SST and MSIT. Darker colours indicate larger correlations, grey denotes correlations that were non-significant ($p > 0.05$ FDR corrected). Between-model correlations are shown within a black box.

Table 1
Group-level descriptive statistics of the main quantitative aspects of the SST. Standard errors are given.

Median go RT (ms)	Median failed stop RT (ms)	Go omissions (%)	Go errors (%)	Mean SSRT (ms)	Median SSD (ms)	Mean stopping accuracy (%)
626 ± 25	543 ± 22	1.9 ± 0.4	2.2 ± 0.4	251 ± 6	350 ± 30	54 ± 1

Table 2
Group-level median RTs and mean accuracies for each condition in the MSIT. Standard errors are given.

	Median RT (ms)	Mean accuracy (%)
CON	536 ± 10	99.3 ± 0.3
SIM	604 ± 12	90.4 ± 1.7
FLA	630 ± 12	95.5 ± 0.8
INC	702 ± 15	78.1 ± 2.5

STN, and SN. For the FS - SS contrast, we observed similar activation patterns as with the former contrast, both cortically and subcortically. For the SS - GO contrast, we found significant cluster differences in four cortical regions; the aI, M1, IFG, and occipital fusiform gyrus, and two subcortical regions; the CN and Tha.

3.3.2. MSIT

3.3.2.2. Task-related activity. For our main measure of interference resolution, the INC – CON contrast, we observe marked differences in recruitment of the ACC, insula, Tha, and VTA (see Fig. 9). We also observe larger recruitment of the ACC and insula in the FLA - CON contrast, but not for the SIM - CON contrast, suggesting these regions are more engaged when resolving the Flanker effect. The SIM - FLA contrast does not display significant differences in activation patterns in the voxel-wise GLMs and is therefore not included in Fig. 9. The contrasts comparing the FLA and SIM conditions to the INC condition display similar differences in the recruitment of the ACC and insula, though to a much lesser extent.

3.3.2.3. Conjunction analysis. To investigate the overlap between response inhibition and interference resolution on a network-level, we calculated a conjunction map between the SS - GO and INC – CON contrasts of the SST and MSIT, respectively. The conjunction map was calculated using the minimum FDR corrected z-score of each contrasts group-level model (see Fig. 10). Notable overlap of activation patterns between the two tasks includes the bilateral aI and rIFG.

3.3.2.4. Subtraction analysis. To observe regions of the brain recruited specifically for response inhibition or interference resolution, we compared the statistically significant activation of the SS - GO contrast from the SST and the INC - CON contrast from the MSIT. Fig. 11 shows significant activation in the INC condition that were not significant in the SS condition (MSIT - SST) and vice versa (SST - MSIT). The MSIT - SST subtraction map indicates a number of significant clusters including the ACC, preSMA, lIFG, anterior supramarginal gyrus (aSG), and Tha. The SST - MSIT subtraction map shows significant activation in the posterior SG (pSG), orbitofrontal cortex, and occipital fusiform gyrus.

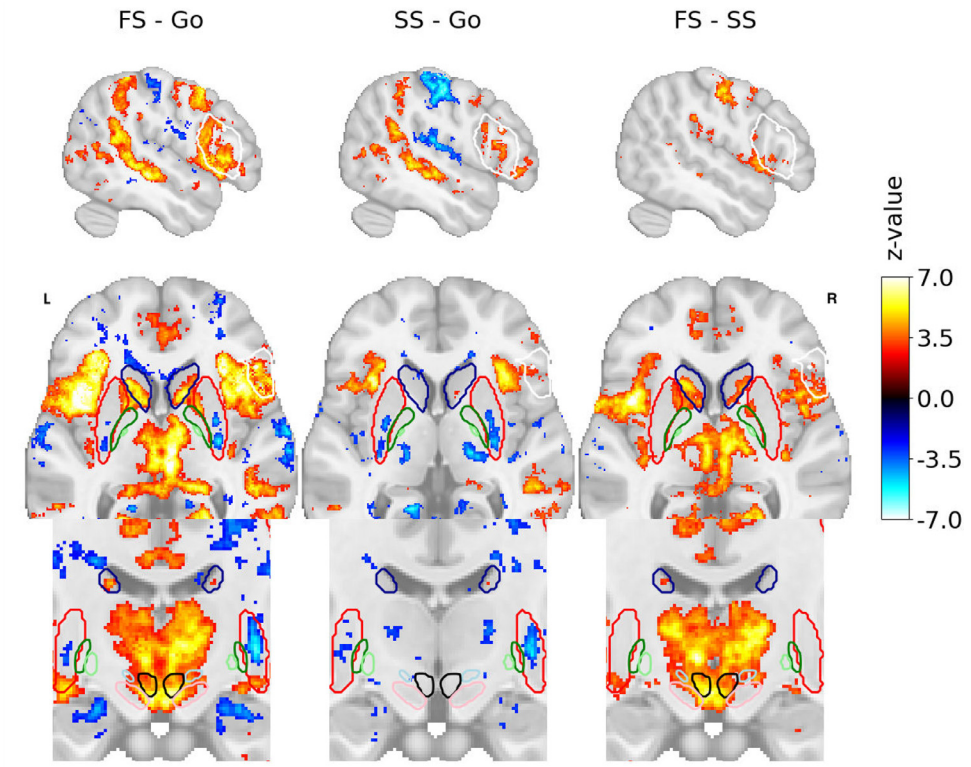

Figure 8. Group-level SPMs of the three main contrasts of the SST. Activation colours indicate FDR thresholded (q < 0.05) z-values. Sagittal (top), axial (middle) and a zoomed in coronal (bottom) view are shown. Coloured contour lines indicate regions of interest (CN in dark blue, PUT in red, STN in light blue, GPe in dark green, GPi in light green, VTA in black, rIFG in white, and SN in pink. The background template and coordinates are in MNI2009c (1mm); slices are drawn through x = 51 (top), y = -13 (bottom), and z = 2 (middle).

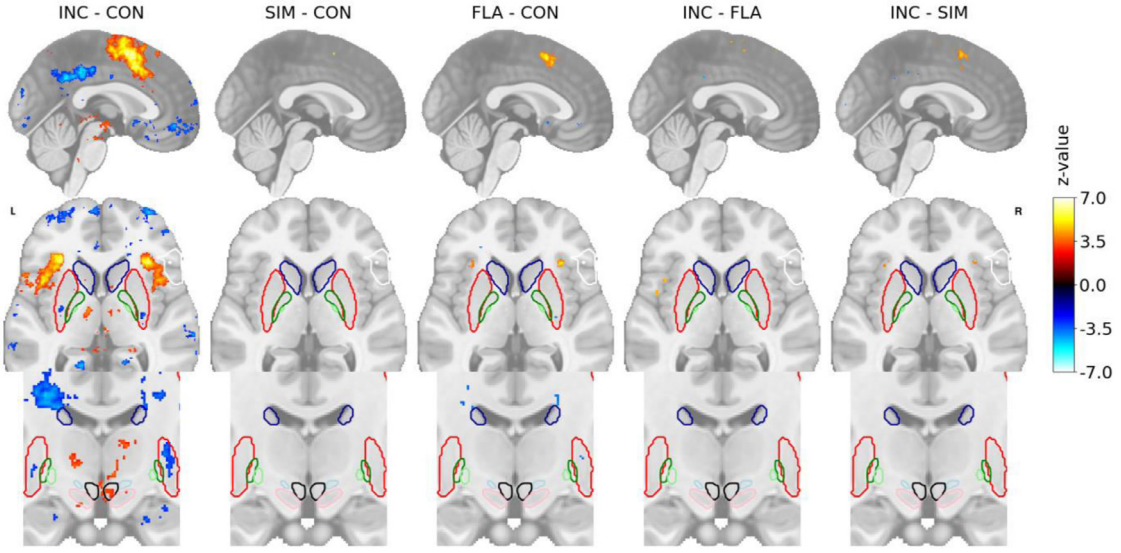

Figure 9. Group-level SPMs of five of the six contrasts of the MSIT. Activation colours indicate FDR thresholded (q < 0.05) z-values. Sagittal (top), axial (middle) and a zoomed in coronal (bottom) view are shown. Coloured contour lines indicate regions of interest (CN in dark blue, PUT in red, STN in light blue, GPe in dark green, GPi in light green, VTA in black, rIFG in white, and SN in pink. The background template and coordinates are in MNI2009c (1mm), where x = 0, y = -13, and z = 2.

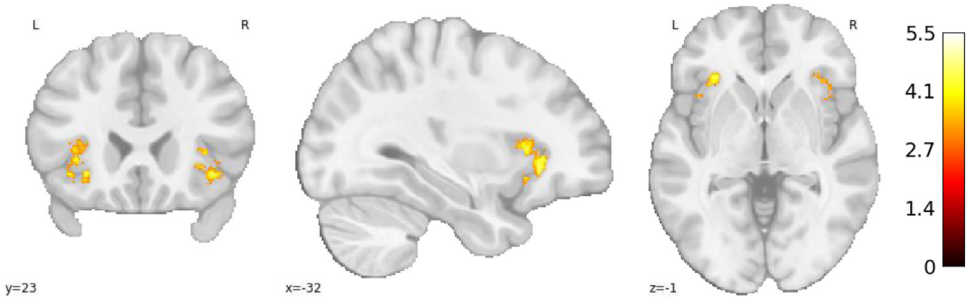

Figure 10. Conjunction analysis between activation from the SS – GO contrast in the SST and INC – CON contrast in the MSIT. Activation colours indicate FDR thresholded (q < 0.05) z-values. The background template and coordinates are in MNI2009c (1mm).

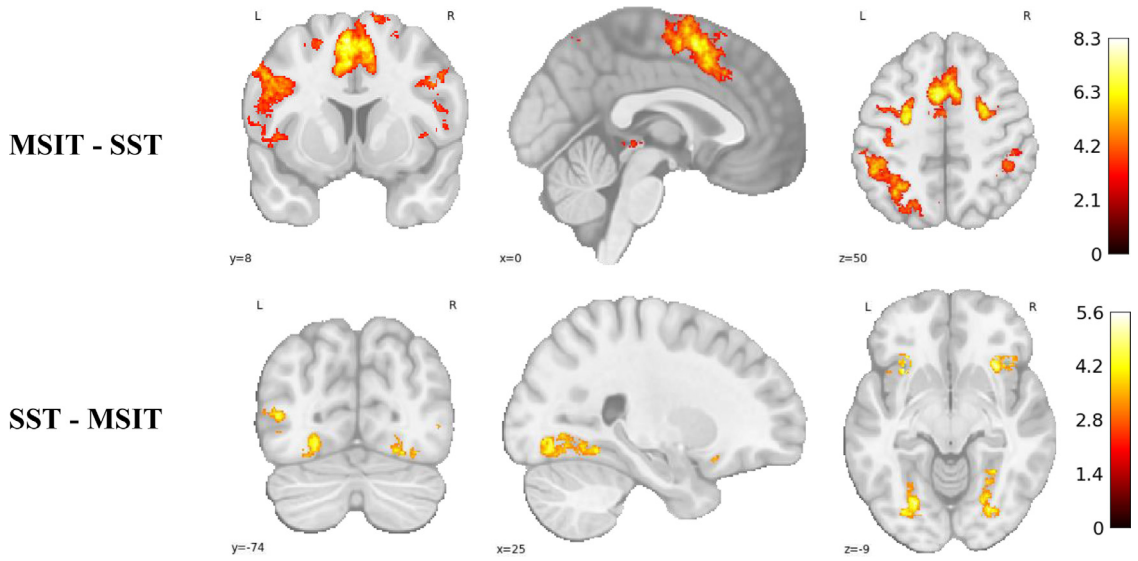

Figure 11. Subtraction analyses between activation from the SS – GO contrast in the SST and INC - CON contrast in the MSIT. The MSIT - SST subtraction map is shown on the top, and the SST - MSIT subtraction map on the bottom. Activation colours indicate FDR thresholded (q < 0.05) z-values. The background template and coordinates are in MNI2009c (1mm).

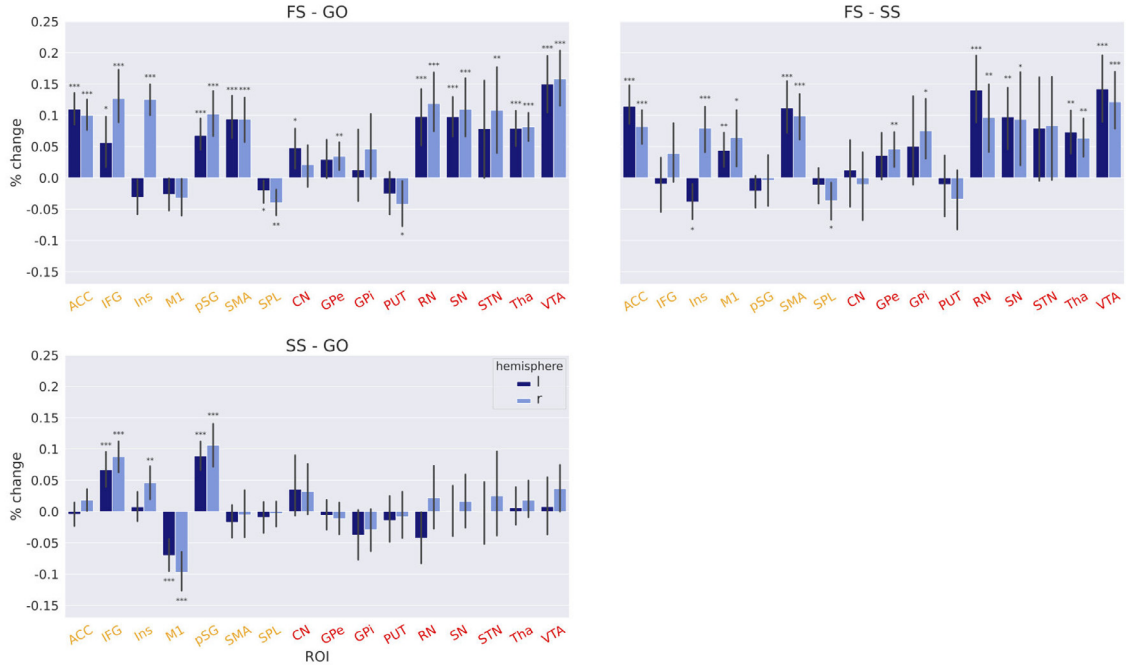

Figure 12. ROI analyses for all contrasts in the SST. The y-axis displays percent signal change and the x-axis, ROIs. T-value significance are FDR corrected (q < 0.05). Error bars depict the 95% confidence intervals for each region. Left hemisphere is shown in dark blue, and right in light blue. Asterisks denotes significance. FS, failed stops; SS, successful stops; ACC, anterior cingulate cortex; IFG, inferior frontal gyrus; Ins, insula; M1, motor cortex 1; pSG, posterior supramarginal gyrus; SMA, pre-supplementary motor area; SPL, superior parietal lobule; CN; caudate nucleus; GPe, globus pallidus externa; GPi, globus pallidus interna; PUT; putamen; RN, red nucleus; SN, substantia nigra; STN, subthalamic nucleus; Str, striatum; Tha, thalamus; VTA, ventral tegmental area. Orange denotes cortical regions, red, subcortical.

3.4. GLMs: ROI analyses

3.4.1. SST

To statistically quantify the different activation patterns within each trial type and contrast of the SST, we fit a set of GLMs using the canonical HRF to the timeseries extracted from each ROI (see Fig. 12). t-values were calculated per run, per ROI for each participant against baseline. In line with previous work (de Hollander et al., 2017; Miletić et al., 2020), significant bilateral STN activation was found in FS and GO trials and right STN activation in SS trials (see Supplementary Fig. 1). Other nodes of the *direct, indirect,* and *hyperdirect* pathways also showed significant activation in all trial types (rIFG, preSMA, aI, SN, and Tha). Turning to the contrasts of interest, we replicated previous findings that showed that FS trials drive a large portion of activation in the subcortex (de Hollander et al., 2017; Miletić et al., 2020). Indeed, the only significant differences in activation found between SS and GO trials in our ROIs were the bilateral IFG, pSG and M1, and right insula. Although SS trials displayed a largely bilateral recruitment of ROIs, the analysis

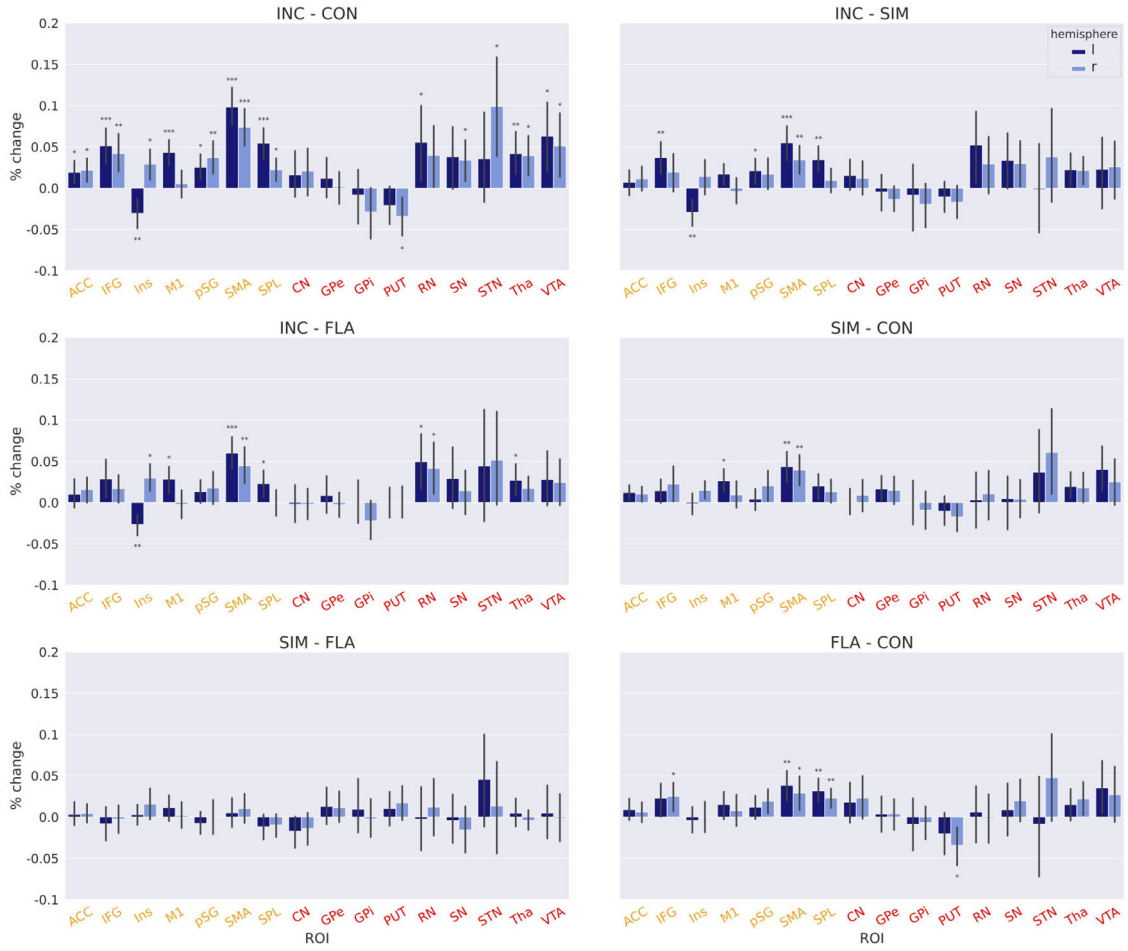

Figure 13. ROI analyses for all contrasts in the MSIT. The y-axis displays percent signal change and the x-axis, ROIs. T-value significance are FDR corrected ($q < 0.05$). Error bars depict the 95% confidence intervals for each region. Left hemisphere is shown in dark blue, and right in light blue. Asterisks denotes significance.INC, incongruent; FLA, Flanker; SIM, Simon; CON, congruent; ACC, anterior cingulate cortex; IFG, inferior frontal gyrus; Ins, insula; M1, motor cortex 1; pSG, posterior supramarginal gyrus; SMA, pre-supplementary motor area; SPL, superior parietal lobule; CN, caudate nucleus; GPe, globus pallidus externa; GPi, globus pallidus interna; PUT, putamen; RN, red nucleus; SN, substantia nigra; STN, subthalamic nucleus; Str, striatum; Tha, thalamus; VTA, ventral tegmental area. Orange denotes cortical regions, red, subcortical.

provided evidence of some type of right-lateralized network in the IFG, insula, GPe, GPi, RN, and STN. In the FS – GO contrast, significantly larger activation was found in the ACC, rIFG, r-insula, pSG, preSMA, lCN, rGPe, RN, SN, rSTN, Tha, and VTA. Both cortically and subcortically, similar activation profiles for the FS – GO and FS – SS contrasts were found, with the notable exception of the IFG, pSG, and lCN which showed similar recruitment on both types of stop trials.

3.4.2. *MSIT*

The same ROI analysis was performed for the MSIT (see Fig. 13). Compared to baseline, all trial types displayed significant activation in most if not all cortical and subcortical ROIs (see Supplementary Fig. 2). Cortically, significant differences in activation between the INC and CON trial types appeared in the ACC, IFG, insula, and preSMA, replicating previous studies of the MSIT (Deng et al., 2018). Subcortically, we found regions that have not been previously observed in this task. Subcortical contribution to the INC - CON contrast included the lRN, rSN, rSTN, Tha, and VTA. All of the INC, SIM and FLA trial types displayed a significant difference in the preSMA from the easiest of the conditions CON, suggesting the cortical region plays an important role in the Simon, Flanker, and joint Simon and Flanker types of interference. For the SIM and FLA conditions, no significant activation differences were found.

3.5. *Model-based analyses*

3.5.1. *SST*

To gain insight into which regions code for inhibition, we correlated ROI-based brain activation with our SST model parameters, zooming in on SSRTs (see Fig. 14). No significant correlations between ROI activity and model parameters were found. We did not replicate previous findings showing a negative correlation between SSRTs and brain activation in SS > GO trials in the STN and the rIFG (Aron & Poldrack, 2006; Li et al., 2006; Whelan et al., 2012). The same is also true when correlating SSRT with brain activity on SS trial or the FS > SS contrast (see Supplementary Fig. 3). In order to compare these results to previous literature, we have also correlated brain activity during the SST with SSRTs calculated using the mean method (Logan & Cowan, 1984; see Supplementary Fig. 4) This method calculates SSRT by subtracting the mean SSD from the mean RT of each individual. When correlating SSRT (calculated by the mean method) with the contrast of SS > GO we do not find any significant correlations, in contention to previous work (Aron & Poldrack, 2006; Li et al., 2006). In addition, as the modelling method of SSRT estimation we use here takes significantly more behavioural information into account, and allows the estimation of the entire distribution of SSRTs, we make inferences only based on these SSRTs, not SSRTs calculated using the mean method.

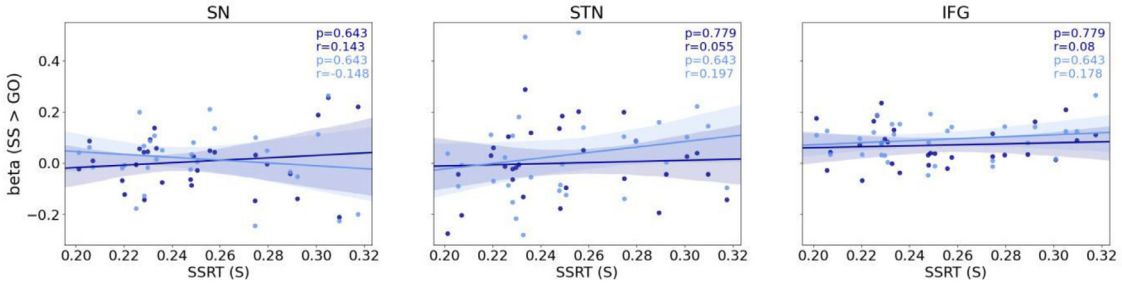

Figure 14. Group-level correlations between GLM betas on the SS > Go contrast and SSRTs in the SST. Significance is FDR corrected. r denotes the Pearson correlation, with *p* the corresponding *p*-value. Left hemisphere is shown in dark blue. Right hemisphere is shown in light blue.

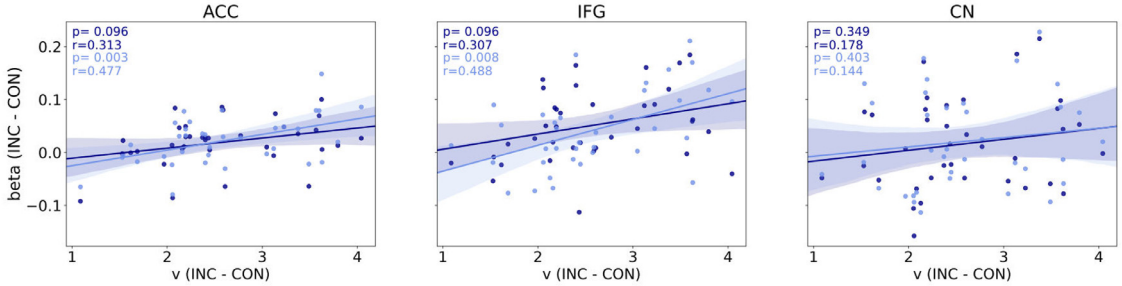

Figure 15. Group-level correlations between GLM betas on INC trials and the drift rate of INC trials in the MSIT. Significance is FDR corrected. p denotes the significance level; r denotes the Pearson correlation. Left hemisphere is shown in dark blue. Right hemisphere is shown in light blue.

3.5.2. MSIT

To observe which regions may code for aspects of interference resolution, we correlated the MSIT model parameters with ROIs that are theorized to be involved in selective inhibition (see Fig. 15). For this, we used the difference in drift rate between the incongruent and congruent conditions, which results in $v_{Simon} + v_{Flank}$ for each participant separately. For our measure of neural activity, we calculated the difference in activation in each ROI on incongruent and congruent trials. After multiple comparison correction, we found that these cognitive model parameters correlated positively with activation in the right ACC and right IFG. We did not find significant correlations in the left ACC, left IFG, or bilateral CN.

4. Discussion

This study aimed to gain insights into the neural and behavioural overlap of response inhibition and interference resolution using a within-subject design. To do so, we tested participants on two tasks, the SST and MSIT, to tap into these subcomponents of inhibition and identify areas of similarities or differences that inter-individual and meta-analytical techniques may miss. Using ultra-high field (UHF) magnetic resonance imaging (MRI), tailored sequences and a high voxel resolution, we were able to obtain robust results, especially in smaller, deeper regions of the brain with a higher SNR than using canonical fMRI at lower fields. Additionally, we used a model-based cognitive neuroscience approach to tap into the latent level of response inhibition and interference control. The results provide evidence of a common network for inhibition-based decision-making as well as the existence of distinctive activation patterns. The whole-brain conjunction map shows that shared activation was found in one central region of the canonical inhibition network, the rIFG, as well as in the aI. Divergent activation regions were found in the main contrast of the MSIT including the ACC, preSMA, lIFG, aSG, and Tha. Inhibition during the SST also involved the recruitment of regions not required for interference resolution, namely the pSG, orbitofrontal cortex (OFC), and occipital fusiform gyrus. The ROI-based analysis is largely in accordance with these whole-brain findings, while suggesting that the posterior division of the supramarginal gyrus may be recruited both in interference resolution and response inhibition.

First, we will discuss the findings of each task separately and compare them to previous task-specific findings before turning to the between-task comparison. For the SST, we replicate recent imaging findings that call into question the idea of the classical inhibitory pathway underlying response inhibition in humans (de Hollander et al., 2017; Jahfari et al., 2011; Miletić et al., 2020; Li et al., 2008). Our whole-brain and ROI analyses indicate that neither the STN, nor any other basal ganglia regions displayed heightened activity when comparing SS trials to GO trials, in contrast to much of the literature on response inhibition (Aron et al., 2014; Aron & Poldrack, 2006; Eagle et al., 2008). A large-scale pattern of greater activation in the basal ganglia nuclei when comparing FS trials to GO trials was observed. This suggests that the act of stopping does not drive the recruitment of the canonical *indirect* or *hyperdirect* pathway, but that activation in these subcortical regions is driven by a failure to inhibit one's actions. Contrasting FS trials with SS and GO trials displays an almost identical network of heightened activity in the ACC, IFG, insula, preSMA, STN, SN, VTA, Tha, and RN. It is however worth noting that SS and GO trials do recruit these nodes when compared to baseline, but to a much lesser extent than FS trials (see Supplementary Fig. 1). Significant bilateral IFG activation was observed when comparing both types of stop trials (FS and SS) to GO trials, suggesting the region may play a role in the detection and integration of the salient stop signal, which is a role that has been theorized before and may not be specific to inhibition tasks (Aron et al., 2004; Hampshire et al., 2009, 2010; Miller & Cohen, 2001; Shallice et al., 2008; Wessel & Aron, 2013). Although it seems that the BOLD response in this region does not differentiate between successful and failed stopping, electrocorticography has shown increased signaling in successful vs failed stopping (Swann et al., 2009; Wessel et al., 2013).

For the MSIT, group-level model estimates of the v_{Simon} and v_{Flank} parameters are comparable, suggesting that participants are equally biased by the Simon and Flanker effects during the task. In addition, the ROI-based analyses observed no differences in activation between the SIM and FLA conditions at the group-level in any ROI, suggesting that these interference types are rooted in similar brain regions and that they

are recruited to a similar degree. Due to the similarity in the two constructs, it may be that a greater number of trials or higher field strength may be required to observe neural differences in their implementation. Contrasting the SIM and FLA conditions with the INC condition display similar responses, with greater activation found in the IFG, preSMA, and SPL for both. For the INC – CON contrast, we observed a marked recruitment of both cortical and subcortical regions that appear to be required for interference resolution. A recent meta-analysis found activation differences in the ACC, preSMA, IFG, insula and putamen when contrasting these conditions (Deng et al., 2018) Here, we replicate these findings as well as provide evidence that a larger network including the SPL, pSG, GPi/e, STN, SN, RN, Tha, and VTA are also activated during interference resolution. In contrast to other previous findings, we did not see significant activation of the CN during interference resolution (Schmidt et al., 2020).

We performed both conjunction and subtraction analyses of the two tasks to observe common and distinct brain areas involved in response inhibition and interference resolution, respectively. The conjunction analysis indicates an overlap in the rIFG and bilateral aI. We do not observe significant differences in lateralization patterns across the two tasks, in contention to previous meta-analytical findings (Isherwood, Keuken, et al., 2021). Multiple regions were identified that are recruited during interference resolution and not response inhibition, namely the ACC, preSMA, lIFG, aSG, and Tha. The ACC and preSMA are highly connected and potentially work together to resolve interference in the environment (Nachev et al., 2008). We also found evidence that the OFC and occipital fusiform gyrus play a role in response inhibition but not interference resolution. Many studies have associated the OFC with the ability to inhibit (Adnan Majid et al., 2013; Eagle et al., 2008; Kringelbach & Rolls, 2004). Although the OFC appears to be recruited during response inhibition, the activation does not appear inhibition-specific as it is observed in a wide variety of roles including value-based decision-making (Montague & Berns, 2002; O'Doherty, 2014), prediction error signaling (Schultz & Dickinson, 2000; Sul et al., 2010) and associative representations (Bechara et al., 1997, 2001). The activation of the occipital fusiform gyrus is usually not associated with response inhibition specifically, but does play a role in colour processing (Bartels & Zeki, 2000). This finding may reflect the presentation of the red stop signal in the SST, as it is the only aspect of the two tasks that differ in colour.

The findings presented here paint a picture of largely divergent networks underlying interference resolution and response inhibition in humans. This demonstrates the need for more intra-individual studies when comparing psychological constructs, owing to the minimization in measurement differences, physiological differences (as all task data is derived on the same day) and the possible impact of large individual variation when using different groups. The extent to which these findings provide evidence for the canonical cortico-basal-ganglia loop is mixed. For the SST, this study provides evidence against the recruitment of the *indirect* or *hyperdirect* pathway during successful response inhibition, as both would implicate increased activity in the STN. These results are in contention to both older and more recent models of response inhibition implementation (Aron et al., 2014; Diesburg & Wessel, 2021; Schmidt & Berke, 2017). Resolution of the combined Simon and Flanker effect does appear to recruit nodes of the *indirect* and *hyperdirect* pathways. The IFG, rSTN, lSN, and Tha are active during interference resolution, but we do not find evidence of the GPe/GPi or striatum in the network, both at a whole-brain and ROI level.

Our model-based analysis of the MSIT revealed that the drift rate difference between INC and CON conditions positively correlated with the difference in activity between INC and CON conditions in the right ACC and right IFG. Since a larger difference in drift rate between the two trial types indicates a greater level of susceptibility to the Simon or Flanker effect, it appears that activity in these two regions somewhat indicate the degree to which participants resolve conflicting stimuli. The ACC has long been suggested to play a role in conflict monitoring (Van Veen & Carter, 2005; Wiecki & Frank, 2013) and these results may indicate that the region encodes the degree of detected conflict. The IFG has been implicated in many roles, but the evidence of drift rate encoding found here suggests it and the ACC are a major requirement for interference resolution. Interestingly, we did not find any evidence of regions encoding for our behavioural measure of response inhibition (SSRT).

Bringing the findings of this study together, it appears that interference resolution and response inhibition recruit markedly separate neural systems. On top of this, the lack of correlation between modelling parameter estimations supports the dissimilarity between processes on a behavioural level. There is therefore little evidence that we should see these two phenomena as two sides of the same inhibition coin. Despite that, the IFG and pSG appear to play a pivotal role in some aspect of both tasks. In view of previous literature, it is likely that the IFG plays a more domain general role in specific types of signal/conflict detection and that it is needed to make the choice of what behavioural step to perform. The continued lack of evidence that the *hyperdirect* and *indirect* pathway are solely engaged in successful response inhibition raises serious concerns. We therefore argue that the pathways involved in successful stopping and successful going are integrated and that the nodes constituting these pathways play task-general roles. Considering that regions of basal ganglia display greater activation for failed stopping, this points towards a general network not specific to global response inhibition.

Data and code availability statements

All code used for preprocessing and analyses of the data acquired in this study can be permanently found on Github, available at the following link: https://github.com/scottyish/Investigating-Intra-Individual-Networks.git

The data acquired in this study will also be uploaded and freely available online (www.figshare.com) after full collection of the database and anonymization is possible.

Declaration of Competing Interest

We have no competing interest to declare regarding this work.

Credit authorship contribution statement

S.J.S. Isherwood: Conceptualization, Data curation, Formal analysis, Investigation, Methodology, Project administration, Validation, Visualization, Writing – original draft, Writing – review & editing. **PL. Bazin:** Conceptualization, Investigation, Methodology, Project administration, Supervision, Writing – review & editing. **S. Miletić:** Data curation, Formal analysis, Investigation, Methodology, Writing – review & editing. **N.R. Stevenson:** Formal analysis, Investigation, Methodology, Software, Writing – review & editing. **A.C. Trutti:** Investigation, Methodology, Project administration, Writing – review & editing. **D.H.Y. Tse:** Data curation, Methodology, Project administration, Writing – review & editing. **A. Heathcote:** Formal analysis, Investigation, Methodology, Software, Writing – review & editing. **D. Matzke:** Formal analysis, Investigation, Methodology, Software, Writing – review & editing. **R.J. Innes:** Formal analysis, Software, Writing – review & editing. **S. Habli:** Data curation, Investigation, Writing – review & editing. **D.R. Sokołowski:** Data curation, Investigation. **A. Alkemade:** Methodology, Writing – review & editing. **A.K. Håberg:** Methodology, Resources, Supervision, Writing – review & editing. **B.U. Forstmann:** Conceptualization, Funding acquisition, Investigation, Methodology, Project administration, Resources, Supervision, Writing – review & editing.

Data availability

Data will be made available on request.

Acknowledgements

We would like to thank PE. Goa for his help with the ongoing collaboration between the University of Amsterdam and the Norwegian University of Science and Technology. This study was supported by a NWO Vici (BUF) and ERC Consolidator Grant (BUF).

Supplementary materials

Supplementary material associated with this article can be found, in the online version, at doi:10.1016/j.neuroimage.2023.119988.

References

Abraham, A., Pedregosa, F., Eickenberg, M., Gervais, P., Mueller, A., Kossaifi, J., Gramfort, A., Thirion, B., Varoquaux, G., 2014. Machine learning for neuroimaging with scikit-learn. Frontiers in Neuroinformatics 8, 14. doi:10.3389/FNINF.2014.00014/BIBTEX, FEB.

Adnan Majid, D.S., Cai, W., Corey-Bloom, J., Aron, A.R, 2013. Proactive selective response suppression is implemented via the basal ganglia. Journal of Neuroscience doi:10.1523/JNEUROSCI.5651-12.2013.

Albin, R.L., Young, A.B., Penney, J.B., 1989. The functional anatomy of basal ganglia disorders. Trends in Neurosciences doi:10.1016/0166-2236(89)90074-X.

Aron, A.R., 2011. From reactive to proactive and selective control: developing a richer model for stopping inappropriate responses. Biological Psychiatry 69 (12), e55. doi:10.1016/J.BIOPSYCH.2010.07.024.

Aron, A.R., Poldrack, R.A., 2006. Cortical and subcortical contributions to stop signal response inhibition: Role of the subthalamic nucleus. Journal of Neuroscience doi:10.1523/JNEUROSCI.4682-05.2006.

Aron, A.R., Robbins, T.W., Poldrack, R.A., 2004. Inhibition and the right inferior frontal cortex. Trends in Cognitive Sciences doi:10.1016/j.tics.2004.02.010.

Aron, A.R., Robbins, T.W., Poldrack, R.A., 2014. Inhibition and the right inferior frontal cortex: One decade on. Trends in Cognitive Sciences doi:10.1016/j.tics.2013.12.003.

Bartels, A., Zeki, S., 2000. The architecture of the colour centre in the human visual brain: new results and a review. The European Journal of Neuroscience 12 (1), 172–193. doi:10.1046/J.1460-9568.2000.00905.X.

Bazin, P.L., Alkemade, A., Mulder, M.J., Henry, A.G., Forstmann, B.U., 2020. Multi-contrast anatomical subcortical structures parcellation. ELife. doi:10.7554/ELIFE.59430.

Bechara, A., Damasio, H., Tranel, D., Damasio, A.R., 1997. Deciding advantageously before knowing the advantageous strategy. Science (New York, N.Y.) 275 (5304), 1293–1295. doi:10.1126/SCIENCE.275.5304.1293.

Bechara, A., Dolan, S., Denburg, N., Hindes, A., Anderson, S.W., Nathan, P.E., 2001. Decision-making deficits, linked to a dysfunctional ventromedial prefrontal cortex, revealed in alcohol and stimulant abusers. Neuropsychologia 39 (4), 376–389. doi:10.1016/S0028-3932(00)00136-6.

Behzadi, Y., Restom, K., Liau, J., Liu, T.T., 2007. A Component Based Noise Correction Method (CompCor) for BOLD and Perfusion Based fMRI. NeuroImage 37 (1), 90. doi:10.1016/J.NEUROIMAGE.2007.04.042.

Birn, R.M., Smith, M.A., Jones, T.B., Bandettini, P.A., 2008. The Respiration Response Function: The temporal dynamics of fMRI signal fluctuations related to changes in respiration. NeuroImage 40 (2), 644. doi:10.1016/J.NEUROIMAGE.2007.11.059.

Bush, G., Shin, L.M., 2006. The Multi-Source Interference Task: an fMRI task that reliably activates the cingulo-frontal-parietal cognitive/attention network. Nature Protocols 1 (1), 308–313. doi:10.1038/NPROT.2006.48.

Bush, G., Shin, L.M., Holmes, J., Rosen, B.R., Vogt, B.A., 2003. The Multi-Source Interference Task: validation study with fMRI in individual subjects. Molecular Psychiatry 8 (1), 60–70. doi:10.1038/SJ.MP.4001217.

Chang, C., Cunningham, J.P., Glover, G.H., 2009. Influence of heart rate on the BOLD signal: The cardiac response function. NeuroImage 44 (3), 857–869. doi:10.1016/J.NEUROIMAGE.2008.09.029.

Cieslik, E.C., Mueller, V.I., Eickhoff, C.R., Langner, R., Eickhoff, S.B., 2015. Three key regions for supervisory attentional control: Evidence from neuroimaging meta-analyses. Neuroscience and Biobehavioral Reviews doi:10.1016/j.neubiorev.2014.11.003.

de Hollander, G., Keuken, M.C., van der Zwaag, W., Forstmann, B.U., Trampel, R., 2017. Comparing functional MRI protocols for small, iron-rich basal ganglia nuclei such as the subthalamic nucleus at 7 T and 3 T. Human Brain Mapping doi:10.1002/hbm.23586.

DeLong, M.R., 1990. Primate models of movement disorders of basal ganglia origin. Trends in Neurosciences 13 (7), 281–285. doi:10.1016/0166-2236(90)90110-V.

Deng, Y., Wang, X., Wang, Y., Zhou, C., 2018. Neural correlates of interference resolution in the multi-source interference task: A meta-analysis of functional neuroimaging studies. Behavioral and Brain Functions doi:10.1186/s12993-018-0140-0.

Diesburg, D.A., Wessel, J.R., 2021. The Pause-then-Cancel model of human action-stopping: Theoretical considerations and empirical evidence. Neuroscience and Biobehavioral Reviews 129, 17–34. doi:10.1016/J.NEUBIOREV.2021.07.019.

Eagle, D.M., Baunez, C., Hutcheson, D.M., Lehmann, O., Shah, A.P., Robbins, T.W., 2008. Stop-signal reaction-time task performance: Role of prefrontal cortex and subthalamic nucleus. Cerebral Cortex doi:10.1093/cercor/bhm044.

Esteban, O., Ciric, R., Finc, K., Blair, R.W., Markiewicz, C.J., Moodie, C.A., Kent, J.D., Goncalves, M., DuPre, E., Gomez, D.E.P., Ye, Z., Salo, T., Valabregue, R., Amlien, I.K., Liem, F., Jacoby, N., Stojić, H., Cieslak, M., Urchs, S., Gorgolewski, K.J., 2020. Analysis of task-based functional MRI data preprocessed with fMRIPrep. Nature Protocols 15 (7), 2186–2202. doi:10.1038/s41596-020-0327-3, *2020 15:7*.

Esteban, O., Markiewicz, C.J., Blair, R.W., Moodie, C.A., Isik, A.I., Erramuzpe, A., Kent, J.D., Goncalves, M., DuPre, E., Snyder, M., Oya, H., Ghosh, S.S., Wright, J., Durnez, J., Poldrack, R.A., Gorgolewski, K.J., 2018. fMRIPrep: a robust preprocessing pipeline for functional MRI. Nature Methods 16 (1), 111–116. doi:10.1038/s41592-018-0235-4, *2018 16:1*.

Frässle, S., Aponte, E.A., Bollmann, S., Brodersen, K.H., Do, C.T., Harrison, O.K., Harrison, S.J., Heinzle, J., Iglesias, S., Kasper, L., Lomakina, E.I., Mathys, C., Müller-Schrader, M., Pereira, I., Petzschner, F.H., Raman, S., Schöbi, D., Toussaint, B., Weber, L.A., Stephan, K.E., 2021. TAPAS: An Open-Source Software Package for Translational Neuromodeling and Computational Psychiatry. Frontiers in Psychiatry 12, 857. doi:10.3389/FPSYT.2021.680811/BIBTEX.

Gelman, A., Hill, J., 2006. Data Analysis Using Regression and Multilevel/Hierarchical Models. Data Analysis Using Regression and Multilevel/Hierarchical Models doi:10.1017/CBO9780511790942.

Gelman, A., & Rubin, D. B. (1992). Inference from Iterative Simulation Using Multiple Sequences. 7(4), 457–472. doi:10.1214/SS/1177011136.

Gilks, W. R., Richardson, S., & Spiegelhalter, D. J. (2003). *Markok Chain Monte Carlo In Practice* (Issue Mm).

Glover, G.H., 1999. Deconvolution of impulse response in event-related BOLD fMRI. NeuroImage 9 (4), 416–429. doi:10.1006/NIMG.1998.0419.

Glover, G. H., Li, T.-Q., & Ress, D. (2000). *Image-Based Method for Retrospective Correction of Physiological Motion Effects in fMRI: RETROICOR*. doi:10.1002/1522-2594.

Greve, D.N., Fischl, B., 2009. Accurate and robust brain image alignment using boundary-based registration. NeuroImage 48 (1), 63–72. doi:10.1016/J.NEUROIMAGE.2009.06.060.

Hampshire, A., Chamberlain, S.R., Monti, M.M., Duncan, J., Owen, A.M., 2010. The role of the right inferior frontal gyrus: inhibition and attentional control. NeuroImage doi:10.1016/j.neuroimage.2009.12.109.

Hampshire, A., Thompson, R., Duncan, J., Owen, A.M., 2009. Selective tuning of the right inferior frontal gyrus during target detection. Cognitive, Affective & Behavioral Neuroscience 9 (1), 103. doi:10.3758/CABN.9.1.103.

Harrison, S.J., Bianchi, S., Heinzle, J., Stephan, K.E., Iglesias, S., Kasper, L., 2021. A Hilbert-based method for processing respiratory timeseries. NeuroImage 230, 117787. doi:10.1016/J.NEUROIMAGE.2021.117787.

Harvey, A.K., Pattinson, K.T.S., Brooks, J.C.W., Mayhew, S.D., Jenkinson, M., Wise, R.G., 2008. Brainstem functional magnetic resonance imaging: disentangling signal from physiological noise. Journal of Magnetic Resonance Imaging : JMRI 28 (6), 1337–1344. doi:10.1002/JMRI.21623.

Heathcote, A., Lin, Y.S., Reynolds, A., Strickland, L., Gretton, M., Matzke, D., 2019. Dynamic models of choice. Behavior Research Methods 51 (2), 961–985. doi:10.3758/S13428-018-1067-Y/FIGURES/15.

Hung, Y., Gaillard, S.L., Yarmak, P., Arsalidou, M., 2018. Dissociations of cognitive inhibition, response inhibition, and emotional interference: Voxelwise ALE meta-analyses of fMRI studies. Human Brain Mapping doi:10.1002/hbm.24232.

Isherwood, S.J.S., Bazin, P.L., Alkemade, A., Forstmann, B.U., 2021. Quantity and quality: Normative open-access neuroimaging databases. PloS One (3) 16. doi:10.1371/JOURNAL.PONE.0248341.

Isherwood, S.J.S., Keuken, M.C., Bazin, P.L., Forstmann, B.U., 2021. Cortical and subcortical contributions to interference resolution and inhibition – An fMRI ALE meta-analysis. Neuroscience and Biobehavioral Reviews doi:10.1016/j.neubiorev.2021.07.021.

Jahanshahi, M., Obeso, I., Rothwell, J.C., Obeso, J.A., 2015. A fronto-striato-subthalamic-pallidal network for goal-directed and habitual inhibition. Nature Reviews. Neuroscience 16 (12), 719–732. doi:10.1038/NRN4038.

Jahfari, S., Waldorp, L., van den Wildenberg, W.P.M., Scholte, H.S., Ridderinkhof, K.R., Forstmann, B.U., 2011. Effective Connectivity Reveals Important Roles for Both the Hyperdirect (Fronto-Subthalamic) and the Indirect (Fronto-Striatal-Pallidal) Fronto-Basal Ganglia Pathways during Response Inhibition. The Journal of Neuroscience 31 (18), 6891. doi:10.1523/JNEUROSCI.5253-10.2011.

Jenkinson, M., Bannister, P., Brady, M., Smith, S., 2002. Improved optimization for the robust and accurate linear registration and motion correction of brain images. NeuroImage 17 (2), 825–841. doi:10.1016/S1053-8119(02)91132-8.

Jenkinson, M., Beckmann, C.F., Behrens, T.E.J., Woolrich, M.W., Smith, S.M., 2012. FSL. *NeuroImage* 62 (2), 782–790. doi:10.1016/J.NEUROIMAGE.2011.09.015.

Kasper, L., Bollmann, S., Diaconescu, A.O., Hutton, C., Heinzle, J., Iglesias, S., Hauser, T.U., Sebold, M., Manjaly, Z.M., Pruessmann, K.P., Stephan, K.E., 2017. The PhysIO Toolbox for Modeling Physiological Noise in fMRI Data. Journal of Neuroscience Methods 276, 56–72. doi:10.1016/J.JNEUMETH.2016.10.019.

Kringelbach, M.L., Rolls, E.T., 2004. The functional neuroanatomy of the human orbitofrontal cortex: evidence from neuroimaging and neuropsychology. Progress in Neurobiology 72 (5), 341–372. doi:10.1016/J.PNEUROBIO.2004.03.006.

Lanczos, C. (1964). Evaluation of Noisy Data. DOI: 10.1137/0701007, 1(1), 76–85. doi:10.1137/0701007

Li, C.S.R., Huang, C., Constable, R.T., Sinha, R., 2006. Imaging response inhibition in a stop-signal task: neural correlates independent of signal monitoring and post-response processing. The Journal of Neuroscience : The Official Journal of the Society for Neuroscience 26 (1), 186–192. doi:10.1523/JNEUROSCI.3741-05.2006.

Logan, G.D., Cowan, W.B., 1984. On the ability to inhibit thought and action: A theory of an act of control. Psychological Review 91 (3), 295–327. doi:10.1037/0033-295X.91.3.295.

Logan, G.D., van Zandt, T., Verbruggen, F., Wagenmakers, E.J., 2014. On the ability to inhibit thought and action: general and special theories of an act of control. Psychological Review 121 (1), 66–95. doi:10.1037/A0035230.

Marques, J.P., Kober, T., Krueger, G., van der Zwaag, W., van de Moortele, P.F., Gruetter, R., 2010. MP2RAGE, a self bias-field corrected sequence for improved segmentation and T1-mapping at high field. NeuroImage 49 (2), 1271–1281. doi:10.1016/J.NEUROIMAGE.2009.10.002.

Marr, D., 1982. Vision: a computational investigation into the human representation and processing of visual information. Vision: A Computational Investigation into the Human Representation and Processing of Visual Information doi:10.1016/0022-2496(83)90030-5.

Matzke, D., Love, J., Heathcote, A., 2017. A Bayesian approach for estimating the probability of trigger failures in the stop-signal paradigm. Behavior Research Methods 49 (1), 267–281. doi:10.3758/S13428-015-0695-8.

Matzke, D., Love, J., Wiecki, T.V., Brown, S.D., Logan, G.D., Wagenmakers, E.J., 2013. Release the BEESTS: Bayesian Estimation of Ex-Gaussian STop-Signal reaction time distributions. Frontiers in Psychology 4. doi:10.3389/FPSYG.2013.00918, DEC.

Matzke, D., Verbruggen, F., Logan, G.D., 2018. The Stop-Signal Paradigm. Stevens' Handbook of Experimental Psychology and Cognitive Neuroscience 1–45. doi:10.1002/9781119170174.EPCN510.

Matzke, D., Wagenmakers, E.J., 2009. Psychological interpretation of the ex-Gaussian and shifted Wald parameters: A diffusion model analysis. Psychonomic Bulletin & Review 16 (5), 798–817. doi:10.3758/PBR.16.5.798, *2009 16:5*.

Miletić, S., Bazin, P.L., Weiskopf, N., van der Zwaag, W., Forstmann, B.U., Trampel, R., 2020. fMRI protocol optimization for simultaneously studying small subcortical and cortical areas at 7 T. NeuroImage doi:10.1016/j.neuroimage.2020.116992.

Miller, E.K., Cohen, J.D., 2001. An integrative theory of prefrontal cortex function. Annual Review of Neuroscience 24, 167–202. doi:10.1146/ANNUREV.NEURO.24.1.167.

Montague, P.R., Berns, G.S., 2002. Neural economics and the biological substrates of valuation. Neuron 36 (2), 265–284. doi:10.1016/S0896-6273(02)00974-1.

Morey, R.D., Rouder, J.N., 2015. Bayesfactor: Computation of Bayes factors for common designs. R package version 0.9.12-2. BayesFactor: Computation of Bayes Factors for Common Designs doi:10.1007/978-3-642-21037-2.

Nachev, P., Kennard, C., Husain, M., 2008. Functional role of the supplementary and pre-supplementary motor areas. Nature Reviews Neuroscience doi:10.1038/nrn2478.

Nee, D.E., Wager, T.D., Jonides, J., 2007. Interference resolution: Insights from a meta-analysis of neuroimaging tasks. Cognitive, Affective, & Behavioral Neuroscience 7 (1), 1–17. doi:10.3758/CABN.7.1.1, *2007 7:1*.

O'Doherty, J.P., 2014. The problem with value. Neuroscience and Biobehavioral Reviews 43, 259–268. doi:10.1016/J.NEUBIOREV.2014.03.027.

Pearson, K., 1895. VII. Note on regression and inheritance in the case of two parents. Proceedings of the Royal Society of London 58 (347–352), 240–242. doi:10.1098/RSPL.1895.0041.

Posse, S., Wiese, S., Gembris, D., Mathiak, K., Kessler, C., Grosse-Ruyken, M.-L., Elghahwagi, B., Richards, T., Dager, S.R., Kiselev, V.G., 1999. Enhancement of BOLD-Contrast Sensitivity by Single-Shot Multi-Echo Functional MR Imaging. Magn Reson Med 42, 87–97. doi:10.1002/(SICI)1522-2594(199907)42:1.

Power, J.D., Mitra, A., Laumann, T.O., Snyder, A.Z., Schlaggar, B.L., Petersen, S.E., 2014. Methods to detect, characterize, and remove motion artifact in resting state fMRI. NeuroImage 84, 320–341. doi:10.1016/J.NEUROIMAGE.2013.08.048.

Ratcliff, R., Murdock, B.B., 1976. Retrieval processes in recognition memory. Psychological Review 83 (3), 190–214. doi:10.1037/0033-295X.83.3.190.

Li, Ray, C, S., Yan, P., Sinha, R., Lee, T.W, 2008. Subcortical processes of motor response inhibition during a stop signal task. NeuroImage doi:10.1016/j.neuroimage.2008.04.023.

Rizk-Jackson, A., Stoffers, D., Sheldon, S., Kuperman, J., Dale, A., Goldstein, J., Corey-Bloom, J., Poldrack, R.A., Aron, A.R., 2011. Evaluating imaging biomarkers for neurodegeneration in pre-symptomatic Huntington's disease using machine learning techniques. NeuroImage 56 (2), 788–796. doi:10.1016/J.NEUROIMAGE.2010.04.273.

Satterthwaite, T.D., Elliott, M.A., Gerraty, R.T., Ruparel, K., Loughead, J., Calkins, M.E., Eickhoff, S.B., Hakonarson, H., Gur, R.C., Gur, R.E., Wolf, D.H., 2013. An improved framework for confound regression and filtering for control of motion artifact in the preprocessing of resting-state functional connectivity data. NeuroImage 64 (1), 240–256. doi:10.1016/J.NEUROIMAGE.2012.08.052.

Schmidt, C.C., Timpert, D.C., Arend, I., Vossel, S., Fink, G.R., Henik, A., Weiss, P.H., 2020. Control of response interference: caudate nucleus contributes to selective inhibition. Scientific Reports 10 (1), 1–15. doi:10.1038/s41598-020-77744-1, *2020 10:1*.

Schmidt, R., Berke, J.D., 2017. A Pause-then-Cancel model of stopping: evidence from basal ganglia neurophysiology. Philosophical Transactions of the Royal Society B: Biological Sciences (1718) 372. doi:10.1098/RSTB.2016.0202.

Schridde, U., Khubchandani, M., Motelow, J.E., Sanganahalli, B.G., Hyder, F., Blumenfeld, H., 2008. Negative BOLD with large increases in neuronal activity. Cerebral Cortex (New York, N.Y. : 1991) 18 (8), 1814–1827. doi:10.1093/CERCOR/BHM208.

Schultz, W., Dickinson, A., 2000. Neuronal coding of prediction errors. Annual Review of Neuroscience 23, 473–500. doi:10.1146/ANNUREV.NEURO.23.1.473.

Sebastian, A., Forstmann, B.U., Matzke, D., 2018. Towards a model-based cognitive neuroscience of stopping – a neuroimaging perspective. Neuroscience and Biobehavioral Reviews 90, 130–136. doi:10.1016/J.NEUBIOREV.2018.04.011.

Sebastian, A., Pohl, M.F., Klöppel, S., Feige, B., Lange, T., Stahl, C., Voss, A., Klauer, K.C., Lieb, K., Tüscher, O., 2013. Disentangling common and specific neural subprocesses of response inhibition. NeuroImage doi:10.1016/j.neuroimage.2012.09.020.

Shallice, T., Stuss, D.T., Alexander, M.P., Picton, T.W., Derkzen, D., 2008. The multiple dimensions of sustained attention. Cortex 44 (7), 794–805. doi:10.1016/J.CORTEX.2007.04.002.

Smith, S.M., Brady, J.M., 1997. SUSAN—A New Approach to Low Level Image Processing. International Journal of Computer Vision 23 (1), 45–78. doi:10.1023/A:1007963824710, *1997 23:1*.

I. R. Stevenson, N.R., I, S.J.S., M, D., H, A., F, B.U, 2022. Latent cognitive mechanisms shared across decision-making domains: A joint modelling approach Unpublished Manuscript.

Sul, J.H., Kim, H., Huh, N., Lee, D., Jung, M.W., 2010. Distinct roles of rodent orbitofrontal and medial prefrontal cortex in decision making. Neuron 66 (3), 449–460. doi:10.1016/J.NEURON.2010.03.033.

Swann, N., Tandon, N., Canolty, R., Ellmore, T.M., McEvoy, L.K., Dreyer, S., DiSano, M., Aron, A.R., 2009. Intracranial EEG reveals a time- and frequency-specific role for the right inferior frontal gyrus and primary motor cortex in stopping initiated responses. The Journal of Neuroscience : The Official Journal of the Society for Neuroscience 29 (40), 12675–12685. doi:10.1523/JNEUROSCI.3359-09.2009.

Swick, D., Ashley, V., Turken, U., 2011. Are the neural correlates of stopping and not going identical? Quantitative meta-analysis of two response inhibition tasks. NeuroImage 56 (3), 1655–1665. doi:10.1016/J.NEUROIMAGE.2011.02.070.

van Maanen, L., Turner, B., Forstmann, B.U., 2015. From model-based perceptual decision-making to spatial interference control. Current Opinion in Behavioral Sciences 1, 72–77. doi:10.1016/J.COBEHA.2014.10.010.

Van Veen, V., Carter, C.S., 2005. Separating semantic conflict and response conflict in the Stroop task: a functional MRI study. NeuroImage 27 (3), 497–504. doi:10.1016/J.NEUROIMAGE.2005.04.042.

Verbruggen, F., Aron, A.R., Band, G.P.H., Beste, C., Bissett, P.G., Brockett, A.T., Brown, J.W., Chamberlain, S.R., Chambers, C.D., Colonius, H., Colzato, L.S., Corneil, B.D., Coxon, J.P., Dupuis, A., Eagle, D.M., Garavan, H., Greenhouse, I., Heathcote, A., Huster, R.J., Boehler, C.N., 2019. A consensus guide to capturing the ability to inhibit actions and impulsive behaviors in the stop-signal task. ELife doi:10.7554/eLife.46323.

Wade, A.R., 2002. The negative BOLD signal unmasked. Neuron 36 (6), 993–995. doi:10.1016/S0896-6273(02)01138-8.

Wessel, J.R., Aron, A.R., 2013. Unexpected events induce motor slowing via a brain mechanism for action-stopping with global suppressive effects. The Journal of Neuroscience : The Official Journal of the Society for Neuroscience 33 (47), 18481–18491. doi:10.1523/JNEUROSCI.3456-13.2013.

Wessel, J.R., Aron, A.R., 2017. On the Globality of Motor Suppression: Unexpected Events and Their Influence on Behavior and Cognition. Neuron 93 (2), 259–280. doi:10.1016/J.NEURON.2016.12.013.

Wessel, J.R., Conner, C.R., Aron, A.R., Tandon, N., 2013. Chronometric electrical stimulation of right inferior frontal cortex increases motor braking. The Journal of Neuroscience : The Official Journal of the Society for Neuroscience 33 (50), 19611–19619. doi:10.1523/JNEUROSCI.3468-13.2013.

Whelan, R., Conrod, P.J., Poline, J.B., Lourdusamy, A., Banaschewski, T., Barker, G.J., Bellgrove, M.A., Büchel, C., Byrne, M., Cummins, T.D.R., Fauth-Bühler, M., Flor, H., Gallinat, J., Heinz, A., Ittermann, B., Mann, K., Martinot, J.L., Lalor, E.C., Lathrop, M., Garavan, H., 2012. Adolescent impulsivity phenotypes characterized by distinct brain networks. Nature Neuroscience doi:10.1038/nn.3092.

Wiecki, T.V., Frank, M.J., 2013. A computational model of inhibitory control in frontal cortex and basal ganglia. Psychological Review doi:10.1037/a0031542.

Woolrich, M.W., Ripley, B.D., Brady, M., Smith, S.M., 2001. Temporal autocorrelation in univariate linear modeling of FMRI data. NeuroImage 14 (6), 1370–1386. doi:10.1006/NIMG.2001.0931.

Yekutieli, D., Benjamini, Y., 1999. Resampling-based false discovery rate controlling multiple test procedures for correlated test statistics. Journal of Statistical Planning and Inference 82 (1–2), 171–196. doi:10.1016/S0378-3758(99)00041-5.

Further reading

Software tools for analysis and visualization of fMRI data - Cox - 1997 - NMR in Biomedicine - Wiley Online Library. (n.d.). Retrieved October 19, 2022, from https://analyticalsciencejournals.onlinelibrary.wiley.com/doi/10.1002/(SICI)1099-1492(199706/08)10:4/5%3C171::AID-NBM453%3E3.0.CO;2-L.